IACMI/0015-2017/3.6

BIG AREA ADDITIVE MANUFACTURING (BAAM) MATERIALS DEVELOPMENT AND REINFORCEMENT WITH ADVANCED COMPOSITES

Authors:
Robert Bedsole
Charles Hill
Kyle Rowe
Chad Duty
Christine Ajinjeru
Vlastimil Kunc
David Riha

Published:
April 24, 2018

PROJECT FINAL REPORT
0015-2017-3.6

Approved for Public Release.
Distribution is Unlimited.

U.S. DEPARTMENT OF ENERGY

THE COMPOSITES iacmi INSTITUTE

FINAL TECHNICAL REPORT

BIG AREA ADDITIVE MANUFACTURING (BAAM) MATERIALS DEVELOPMENT AND REINFORCEMENT WITH ADVANCED COMPOSITES

Robert Bedsole
Charles Hill
Kyle Rowe
Chad Duty
Christine Ajinjeru
Vlastimil Kunc
David Riha
713-542-0109
chill@localmotors.com

Project Period: 09:2016-06:2017
Date Published: April 2018

Prepared by
Institute for Advanced Composites
Manufacturing Innovation
Knoxville, Tennessee 37932
managed by
Collaborative Composite Solutions, Inc.
for the
US DEPARTMENT OF ENERGY
under contract DE- EE0006926

CONTENTS

LIST OF FIGURES

LIST OF TABLES

ACKNOWLEDGEMENTS

The information, data, or work presented herein was funded in part by the Office of Energy Efficiency and Renewable Energy (EERE), U.S. Department of Energy, under Award Number DE-EE0006926 with the Institute for Advanced Composites Manufacturing Innovation (IACMI).

The project would like to acknowledge the support of the DOE and IACMI for providing the funding and collaborative environment that is enabling composite materials and process innovation across a variety of large volume applications. Also, the Oak Ridge National Laboratory and its Manufacturing Demonstration Facility have been exceptionally accessible as a technology development partner and continue to provide access to the highest caliber equipment and personnel.

Local Motors would like to thank our management team and investors for supporting this work and appreciating the value of materials and processes in bringing disruptive hardware to market

1. EXECUTIVE SUMMARY

Additive manufacturing (AM) by extrusion deposition is rapidly developing as an energy efficient process that greatly reduces development time for new products including vehicle structures. Development of reinforced thermoplastic compounds that are specifically tailored to the AM process and possess the properties necessary for engineering structures is currently underway. This project focused on developing a fundamental understanding of printability by performing a number of polymer characterization tests, initial printability screenings, and basic mechanical property determinations for a number of compounds. Structural evaluations of more complex printed articles were also performed in order to build a database of mechanical performance for validation of structural simulations planned for Phase II. Included in the structural tests were components that were reinforced using a number of methods including over-wrapping with dry fabric and resin infusing to form an advanced composite having the shape of the 3D printed structure. The results indicate a number of factors that affect printability of materials, and initial structural analysis shows that the data generated will be useful for model validation.

1.1 BACKGROUND

Large scale 3D printing has been demonstrated through several successful project collaborations between Local Motors and Oak Ridge National Laboratory, both of which have made significant investments to advance this technology out of the development stage and toward the commercial deployment of 3D printed automobiles and related products. The low-cost, energy efficient manufacturing techniques of Local Motors will likely include recyclable discontinuous carbon fiber and thermoplastic resin. Such material systems are of particular interest to IACMI, and the continued innovation of large scale 3D printing will help IACMI partners reach their goal of lowering energy consumption and greenhouse gas emissions while accelerating the realization of life cycle energy efficiency targets for fiber-reinforced polymer composite applications in vehicles.

In traditional manufacturing, a part is created by either removing material from a billet (milled, lathed, cut, etc.) or shaped using a tool (injection molding, pressing, forming, etc.). These methods require a significant investment of time and energy, both of which are directly related to cost. Because traditional manufacturing either relies on creating and then subsequently removing material, or requires complex tooling to produce a desired geometry, its efficiency is less than optimal. By placing material exactly where it is needed, without the help of complex tools or dies, manufacturing efficiency can approach ideal levels. Local Motors is committed to the design, manufacture, and marketing of vehicles produced using large-scale extrusion deposition so that the design cycle time may be drastically reduced (50%), and multiple vehicle styles may be produced simultaneously from the same micro-factory. The process also represents a vast reduction in embodied energy (37%) and carbon emissions (52%), and results in a recycle-able structure (compared to traditional manufacturing methods). The materials and processes developed are also applicable across many manufacturing sectors and are universal developments that will increase production efficiency and reduce the carbon footprint of a wide variety of product types.

- 50% reduction in design to manufacturing cycle time
- 37% decrease in embodied energy
- 52% fewer carbon emissions

There are several key challenges and risks in the development of a vehicle manufactured primarily by additive processes using direct digital manufacturing (DDM). Materials initially available had mechanical properties that limited vehicle design and had questionable long-term performance in expected environments. New materials are sought which have improved mechanical properties, while

also demonstrating appropriate chemical resistance and temperature performance.

1.2 RESULTS AND DISCUSSION

Technical work was focused on new materials development for the BAAM (big area additive manufacturing) system. A baseline characterization methodology was employed to establish print conditions and print test samples for mechanical testing. Tensile testing was performed to understand the effects of different resin and filler combinations on the mechanical properties of AM parts. Rheological testing and thermal analysis were used to collect data on physical properties in order to better understand differences between materials and understand what properties enable improved printability.

In addition to new material development, affordable manufacturing techniques to reinforce additively manufactured (AM) structures will also be investigated. A simple beam specimen envelope (representative of a floor or wall section from the Strati [1]) was chosen in order to quantitatively compare a variety of reinforcement techniques including foam filling, overwrapping with continuous fibers, metal insertion, and 3D printed infill. A previous publication by Local Motors [2] included torsion tests of 11 different structural sub-elements printed on a developmental machine [3]; the current work expands upon this to include torsion, bending, and shear tests of 32 different samples. These parts were printed on a commercially-available large-scale extrusion deposition printer (Cincinnati BAAM) in order to obtain more consistent bead width. Thermal imaging was used to ensure better consistency of layer-to-layer adhesion in each print. The results of these tests will be used to communicate design possibilities to automotive designers and will also provide a means to verify FEA models of a wide variety of reinforced additive manufacturing structures.

1.2.1 Theoretical Framework

The large scale extrusion deposition process as implemented by the Cincinnati BAAM (Figure 1) utilizes a pellet feed system to convey material to a single screw extruder on an X,Y,Z gantry manipulator to form a product in a layer-by-layer fashion. Figure 2 illustrates this printing process, along with the global BAAM machine coordinate system (x,y,z), as well as the local coordinate system (x’,y’,z’) where x’ is the direction of printing.

Figure 1. Photograph of Cincinnati BAAM Machine.

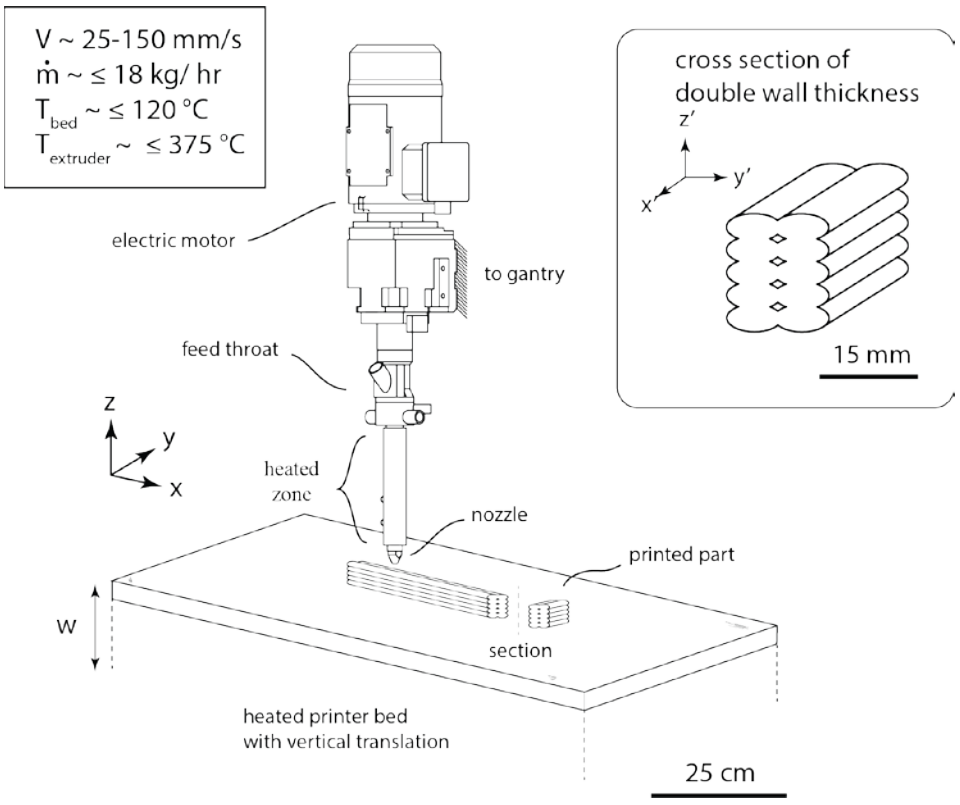

Figure 2. Illustration of BAAM process with global x,y,z printer directions and local x',y',z' print directions identified. x' is the direction of printing.

1.2.2 Material Characterization

What was the purpose of materials characterization: e.g. select materials for structural testing, determine lowest cost combination suitable for structural use.

All materials were dried according to manufacturer recommendations prior to printing. Extruder temperature profiles for each material were chosen based on industry recommendations for injection molding. All materials were printed on textured ABS sheets attached by vacuum to a 100°C table. All initial material evaluation prints were conducted at 5 in/sec with no dynamic gantry accelerations or extruder serving in order to eliminate those effects on measured bead width variations. Single-wall thickness hexagons (864 mm diameter inscribed circles) were initially printed 3 layers tall (11.4 mm), and the extrusion rate was adjusted for each of these preliminary prints in order to obtain a minimum top layer bead width of 10.2 mm, with a desired average bead width of ~11.4 mm. Once the extrusion rate was chosen, a 305 mm tall hexagon was printed for mechanical evaluation.

All hexagon prints included programmed pauses between layers in order to allow enough cooling time for structural rigidity before printing the next layer. These interlayer pauses were followed by 7 second purges of material to eliminate the possibility that the material may have suffered some level of thermal degradation at the hottest end of the extruder. Thermal images were recorded at 30 Hz during each print for the evaluation of cooling rates. All printing parameters were also recorded for future reference.

1.2.2.1 Tension

1.2.2.1.1 Tension Procedures

Twelve different materials were printed as single-wall hexagons (864 mm diameter inscribed circles, 305 mm tall). After printing, parts were allowed to cool until the build table reached 50°C. After at least 24 hours, the six sides were cut into planks using a circular saw. The bead cusps on the front and back of planks were then removed with a planer (DeWALT® DW735 planer with a Byrd Tool® Shelix® cutter head). Surface roughness due to machining was removed using light abrasive sanding with 80 grit sandpaper and a dual action palm sander; dogbone shapes were subsequently machined on a CNC router using a DLC (diamond-like carbon) coated end mill. Typically, z'-direction (stacking direction, see Figure 2) dogbones were machined from the 3rd wall (in the order of printing), and x'-direction (print direction, see Figure 2) dogbones were machined from the 4th and 5th walls. The tensile testing specimen geometry was chosen to be an ASTM Type III coupon that was scaled to be two times (2X) larger than the standard (Figure 3). The overall length was then shortened to be 304.8 mm by removing length from the gripped portion of the sample. These modifications were made to the sample geometry to increase the number of printed beads within the gage section of the sample. With a 3.8 mm layer height, x'-direction samples contained ten printed beads as opposed to a standard size specimen which would only include five, thus providing a better average of mechanical performance. z'-direction samples contained 30 beads within the gage length.

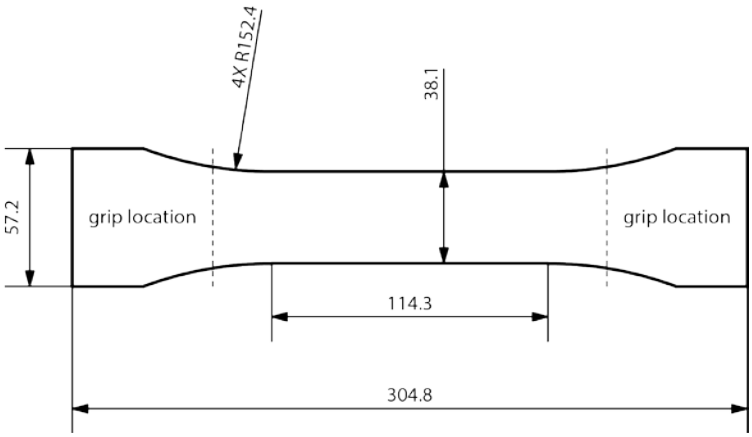

Figure 3. The tensile specimen geometry that was adopted for testing large scale additively manufactured structures is an ASTM Type III geometry that was scaled to be two times (2X) larger. To reduce the effects of the stress concentrations at the sample radii, the specimen was gripped inside of the radius for testing (~63 mm from the ends of the sample).

Mechanical testing was performed on an Instron™ 1330 servo-hydraulic load frame, with a 250 N capacity, hydraulic wedge grips, and digital controls. Tensile tests were performed for each material in both the print (x'-direction) and stacking direction (z'-direction). Experiments were performed under displacement control with a displacement rate of 31.5 µm/s for x'-direction samples and 15.7 µm /s for z'-direction samples. Strain was calculated from measurements taken with an Epsilon™ model 3542 axial extensometer with a 25.4 mm gage length, and force measurements were made with an Instron™ 250 N load cell. All data was acquired at 10 Hz.

1.2.2.1.2 Tension Results

All tensile results are summarized in Figure 4. Error bars indicate one standard deviation from the mean. Each bar represents the mean of at least three gage failures. A minimum of three gage failures was

established for evaluating screening level mechanical properties. These results are discussed in detail in the following sections.

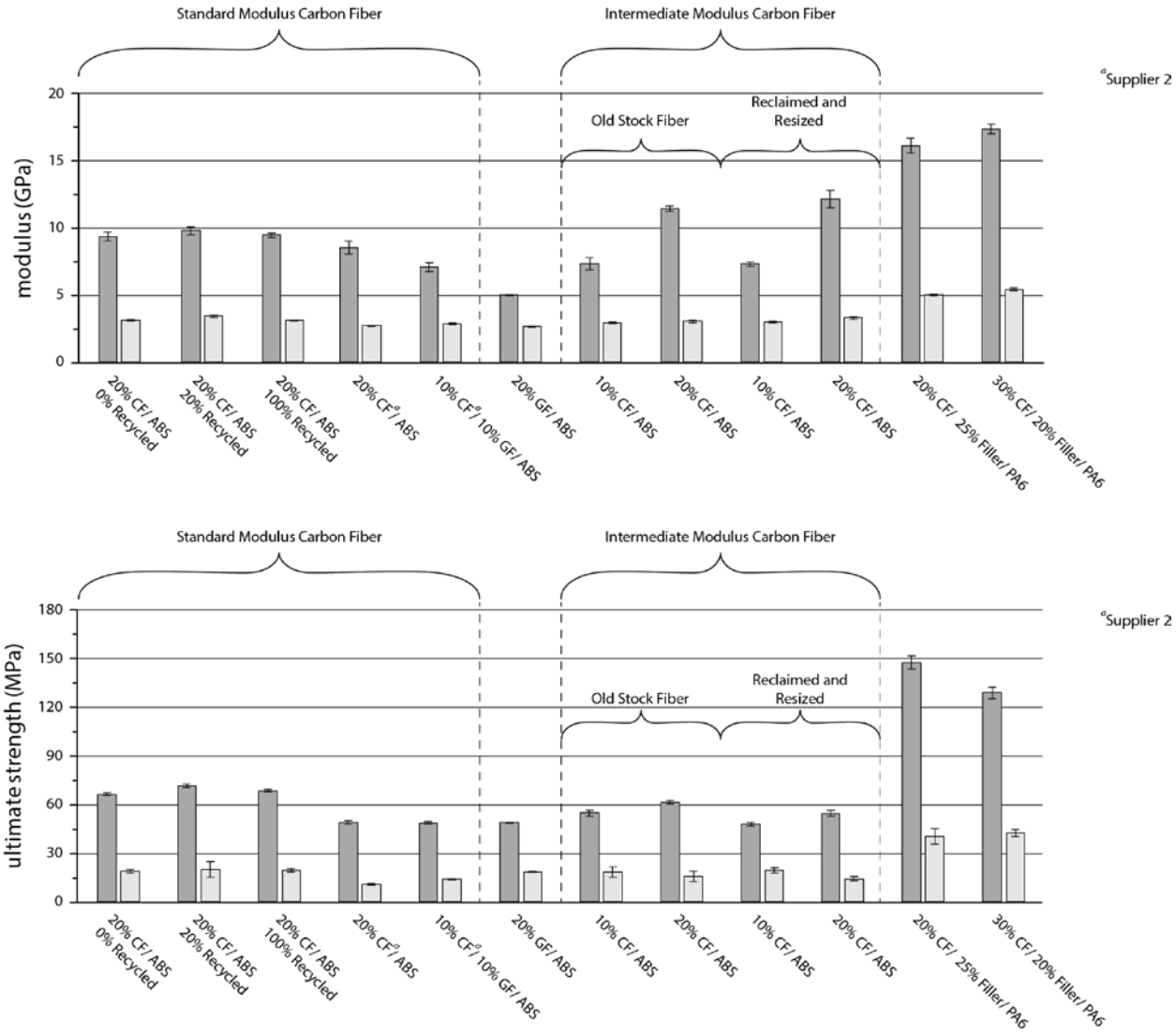

Figure 4. Complete project tension results. Error bars indicate one standard deviation from the mean.

Recycling AM Materials

Table 1 Tensile Properties of Recycled CF/ ABS by Additive Manufacturing.

			Filler 1		X-direction		Z-direction	
Sample #	**Recycled: Virgin (%)**	**Base Resin**	**Type**	**Amount**	**E (GPa)**	**UTS[2] (MPa)**	**E (GPa)**	**UTS (MPa)**
1	0:100	ABS	SMCF[1]	20%	9.35	66.0	3.09	18.7
2	20:80	ABS	SMCF[1]	20%	9.77	71.1	3.39	19.6
3	100:0	ABS	SMCF[1]	20%	9.44	68.0	3.07	19.1

[1] SMCF = Standard Modulus Carbon Fiber (superscript denotes Supplier #)

[2] UTS = Ultimate Tensile Strength

Additive manufacturing (AM) with thermoplastics allows for inexpensive recycling by grinding and re-compounding material that has previously been 3D printed. This process involves additional thermal cycling and fiber breakage compared to virgin material; therefore, mechanical properties are expected to decrease. However, it has been hypothesized that mixing a small amount of regrind with virgin material may actually improve mechanical properties due to an optimal distribution of longer and shorter carbon fiber.

Printed parts using 20 wt% carbon fiber-filled ABS (CF/ ABS) were collected, ground, and compounded with virgin CF/ ABS at several different ratios (Table 1). Figure 5 compares the elastic modulus and ultimate strength of virgin CF/ ABS (0% regrind), 20% regrind + 80% virgin CF/ ABS (20% regrind), and 100% regrind in the x' and z'-directions. As predicted, there are small improvements in the modulus and strength of 20% regrind compared to the control. Surprisingly, there was no decrease in mechanical properties when comparing 100% recycled to 100% virgin material. These results warrant further investigation, including a complete mapping of the space between 20% and 100% regrind. Future work will likely also include a study of the number of cycles of 100% regrind before significant reduction in mechanical properties is measured, as well as recyclability studies of other printed materials.

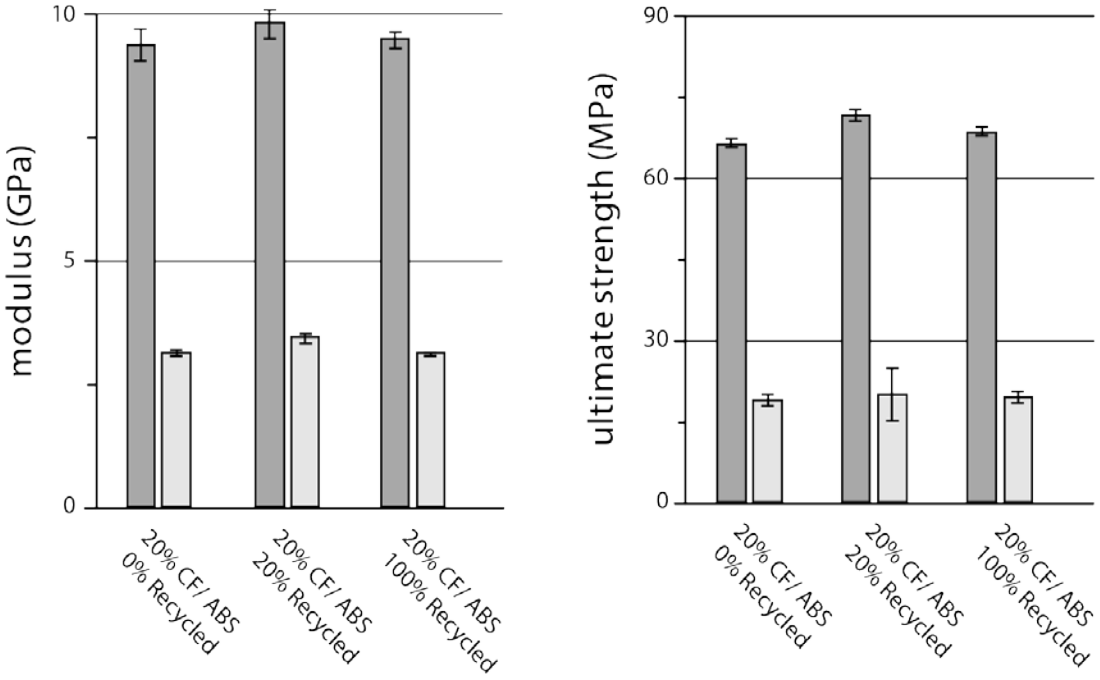

Figure 5. Tension results for 20% CF/ ABS: 100% virgin, 20% recycled, and 100% recycled. Error bars indicate one standard deviation from the mean.

Compounding with Virgin and Reclaimed Fiber

Because CF/ ABS has been previously found to be highly printable, and its properties have been examined thoroughly [1,4-7], seven different formulations with this ABS base resin were compounded using different fibers; these are compared in Table 2 with 0% regrind as a reference. Samples 4-6 included virgin fibers. Fibers used in samples 7-8 were out-of-date. Fibers used in samples 9-10 were reclaimed and resized.

Table 2 Tensile Properties of ABS Reinforced with Virgin and Reclaimed Fiber by AM.

		Filler 1		Filler 2		X-direction		Z-direction	
Sample #	**Base Resin**	**Type**	**Amount**	**Type**	**Amount**	**E (GPa)**	**UTS (MPa)**	**E (GPa)**	**UTS (MPa)**
1	ABS	SMCF[1]	20%	-	-	9.35	66.0	3.09	18.7
4	ABS	SMCF[1]	20%	-	-	8.51	48.6	2.70	10.4
5	ABS	SMCF[1]	10%	GF	10%	7.03	48.3	2.84	13.7
6	ABS	GF	20%	-	-	4.95	48.5	2.65	18.2
7	ABS	IMCF[2]	10%	-	-	7.31	54.3	2.88	17.8
8	ABS	IMCF[2]	20%	-	-	11.42	61.0	3.02	15.5
9	ABS	IMCF[2]	10%	-	-	7.29	47.5	2.98	19.1
10	ABS	IMCF[2]	20%	-	-	12.12	54.1	3.26	14.0

[1] SMCF = Standard Modulus Carbon Fiber (Superscript denotes Supplier #)

2 IMCF = Intermediate Modulus Carbon Fiber (superscript denotes Supplier #)

3

When standard modulus carbon fiber from Supplier 2 replaced the carbon fiber in the control (Sample 4), there were large reductions in tensile properties compared to the control (Sample 1); these results (Figure 6) were likely due to a difference in sizing. As this carbon fiber was replaced by glass fiber (Samples 5-6), there was a linear reduction in x'-direction modulus; however, there was very little difference in x'-direction ultimate strength or z'-direction tensile modulus between Samples 5 and 6. Replacing the control (Sample 1) carbon fiber with the same weight percentage of reclaimed intermediate modulus fibers (Samples 8 & 10) caused a significant increase in x'-direction modulus but a significant decrease in ultimate strength in both x'- and z'-directions. Replacing the 20% by weight standard modulus carbon fibers in the control (Sample 1) with only 10% by weight reclaimed IMCF (Samples 7&9) caused an insignificant increase in z'-direction ultimate strength but a significant reduction in x'-direction tensile properties.

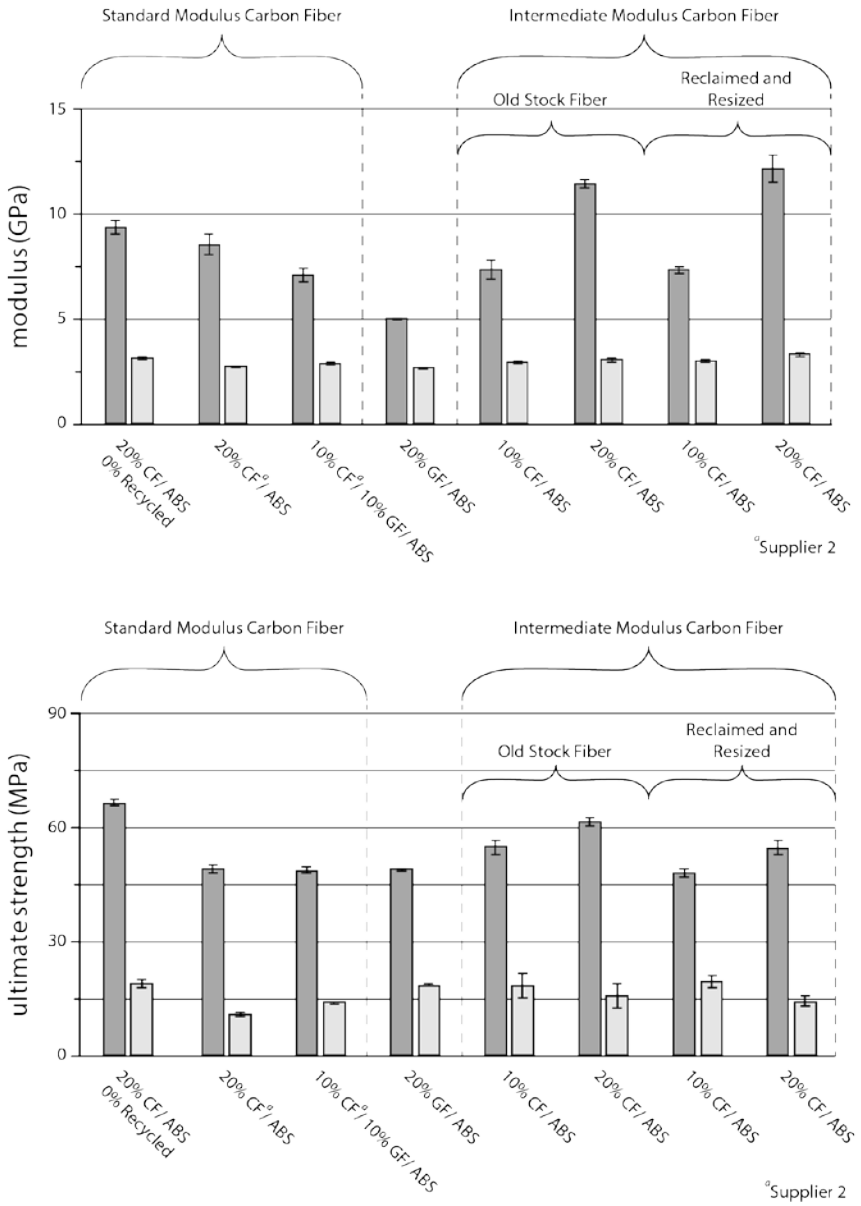

Figure 6. Tension results for ABS resin compounded with various virgin and recycled fibers. Error bars indicate one standard deviation from the mean.

Improving Mechanics by Changing the Base Resin

To significantly improve the x'- and z'-direction tensile properties of AM prints, PA6 (polyamide 6) was substituted as the base resin. Two formulations (Table 3) had approximately twice the x'-direction modulus, 1.5x the z'-direction modulus, twice the x'-direction ultimate strength, and twice the z'-direction ultimate strength compared to Sample 1 (Figure 7). Unlike Sample 1 (CF/ ABS), Sample #12 thinned significantly within each layer of the print, and both PA6 samples (11-12) deformed significantly during printing; these issues were investigated using rheology (Section 1.3.2.2), thermo-mechanical analysis (Section 1.3.2.3), and further printability assessment with complex geometry (Section 1.3.2.4).

Table 3 Tensile Properties of ABS and PA6 Base Resins by AM.

		Filler 1		Filler 2		X-direction		Z-direction	
Sample #	**Base Resin**	**Type**	**Amount**	**Type**	**Amount**	**E (GPa)**	**UTS (MPa)**	**E (GPa)**	**UTS (MPa)**
1	ABS	SMCF[1]	20%	-	-	9.35	66.0	3.09	18.7
11	PA6	SMCF[1]	20%	Prop[2]	25%	16.11	146.9	4.96	40.0
12	PA6	SMCF[1]	30%	Prop[2]	20%	17.33	128.2	5.39	42.1

[1] SMCF = Standard Modulus Carbon Fiber (superscript denotes Supplier #)
[2] Prop = Proprietary

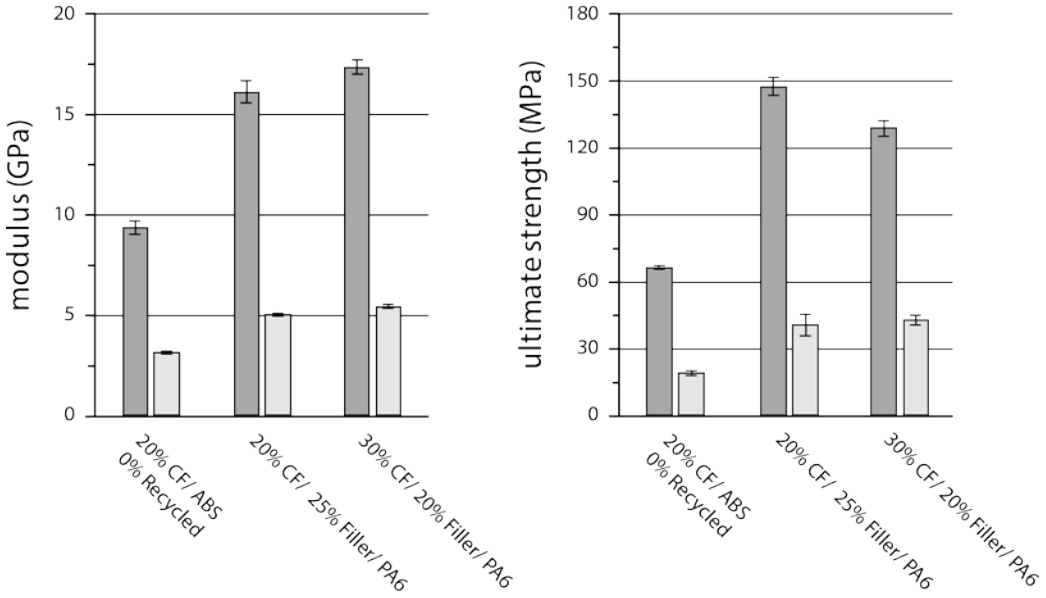

Figure 7. Tension results comparing ABS and PA6 base resins. Error bars indicate one standard deviation from the mean.

1.2.2.2 Rheology

It was noted that parts printed with ABS as the base resin always printed consistently on the BAAM (<10% bead width variation when measuring the bead width at the center of each wall of the hexagon); however, polyamides were much more variable. Sample #11 printed with similar consistency to the ABS hexagons, whereas Sample #12 thinned significantly (>20%) when comparing the first and last walls of the hexagon. Additionally, a filled PA66 (polyamide 66) printed with bead width consistency similar to CF/ ABS. In order to better understand this aspect of overall printability, parallel plate rheology was performed on each of these samples.

1.2.2.2.1 Rheology Procedures

Rheological characterization of the candidate materials was conducted using a Discovery Hybrid Rheometer-2 (DHR-2) from TA Instruments. The materials were dried in pellet form according to the conditions shown in Table 4 prior to testing. Pellets were loaded between two parallel plates with a diameter of 25 mm and heated to the test temperature in air. Once melted, the gap was maintained between 1.5 mm and 2.5 mm for all the samples during testing. The materials were subjected to an oscillatory shear strain of 0.5% to remain within the linear viscoelastic region. The oscillatory frequency was varied

between 0.1 and 100 rad/s to approximate the shear rates experienced during BAAM extrusion (roughly 10-100 1/s following the Cox-Merz Rule). The complex viscosity (η*) was measured as a function of oscillation frequency (ω) as well as the storage modulus (G') and loss modulus (G") of the material. The materials were evaluated at a representative "hot" and "cold" temperature that differed by 20°C to determine the effect of processing temperature. In one instance, the thermal stability of the material was evaluated at a constant temperature by observing the change in viscosity over time (~15 minutes at a strain rate of 0.5% and an oscillation frequency of 1 Hz). The rheological testing conditions are shown in Table 4 below.

Table 4 Candidate Materials for Rheological Testing.

		Filler 1		Filler 2				
Sample #	**Base Resin**	**Type**	**Amount**	**Type**	**Amount**	**Drying Conditions**	**Sweep Type**	**Temps** °C
1	ABS	CF	20%	-	-	2 hrs @ 77°C	Freq	230 250
11	PA6	CF	20%	Prop*	25%	2 hrs @ 77°C	Freq	270 290
							Time	270
12	PA6	CF	30%	Prop*	20%	3 hrs @ 77°C	Freq	270 290
13	PA66	CF	10%	GF	20%	3 hrs @ 77°C	Freq	270 290

* Prop = Proprietary

1.2.2.2.2 Rheology Results

The rheological results for the candidate materials are summarized in Table 5 below, and plots of rheological parameters as a function of shear rate and time are given in Appendix A. The viscosity (η), storage modulus (G'), and loss modulus (G") are listed for each material at an oscillation frequency of 100 /s, which is generally within the range of shear rate experienced at the exit of the BAAM extruder. Each of the variables are listed for the two processing temperatures considered, and the corresponding change in value is calculated as the processing temperature increases. It can be generally observed that the rheological properties of all the materials decrease by roughly 20-30% with a 20°C increase in temperature. With regards to BAAM processing, this trend highlights the importance of temperature control for consistent performance and also identifies temperature as a relevant parameter for intentionally altering the flow characteristics during a build. The viscosity of the materials at the processing temperature is typically in the range of 1 kPa-s at a shear rate of 100/s. The storage modulus demonstrated a slightly larger range, with the ABS material having a G' in the range of 150 kPa while the remaining polyamide materials were in the range of 30-45 kPa. The loss modulus (G") was slightly more consistent across the sample materials, roughly in the range of 100 kPa with the exception of Sample 13. It should be noted that for all of the polyamide materials, the loss modulus typically exceeded the storage modulus by a margin of 2-3x, whereas the storage modulus of Sample 1 was slightly higher than the loss modulus. During BAAM deposition, a material with a dominant loss modulus will likely demonstrate less die swell, a longer relaxation time, and therefore a potentially more consistent bead geometry.

Table 5 . Rheological properties at oscillation frequency of 100 rad/s.

Sample #	Temp (°C)	Viscosity (η)		Storage Modulus (G')		Loss Modulus (G")	
		(Pa s)	% Change	(Pa)	% Change	(Pa)	% Change
1	230ºC	2,124	-26%	168,237	-26%	129,609	-25%
	250ºC	1,579		124,357		97,334	
11	270ºC	1,002	-32%	27,883	-25%	96,248	-33%
	290ºC	678		20,785		64,545	
12	270ºC	1,288	-16%	45,225	-14%	131,047	-23%
	290ºC	1,084		39,035		101,114	
13	270ºC	966	-21%	49,713	-9%	82,822	-26%
	290ºC	760		45,289		60,992	

The characteristic shear thinning behavior of thermoplastics is typically described using a power law relation: $= C\ \dot{\gamma}^{(n-1)}$, where the viscosity (η) is an exponential function of the shear rate ($\dot{\gamma}$), C is a constant, and n is the power law index. This is especially critical for BAAM deposition since a polymer will likely experience 3-4 orders of magnitude difference in shear rate as it passed through the single screw extruder ($\sim$5000 s^{-1}), out the nozzle ($\sim$100 s^{-1}), and during deposition (0.1 to 10 s^{-1}). The change in viscosity over an order of magnitude difference in shear rate is demonstrated for the candidate materials in Table 6 below. The table lists the complex viscosity (η*) of the materials at an oscillation frequency of 10/s and 100/s, which roughly approximates the shear rate experienced by the polymer during exit from the BAAM nozzle and deposition of the bead on the previously deposited material. As in Table 5 above, the change in viscosity due to temperature is calculated for each material. In general, the viscosity decreases with temperature for all materials, but the effect is more pronounced at higher shear rates. The last column in Table 6 shows the shear thinning effect by comparing the viscosity at 10/s to that at 100/s. In general, the viscosity of each of the materials is observed to decrease by 50-75% as the shear rate increases from 10/s to 100/s. Since the shear rate of an extruded material through a circular orifice is linearly dependent on the volumetric flow rate and scales inversely with the cube of the orifice radius, a relatively small change in the extrusion die geometry can have a significant impact on the apparent shear rate, and thus the rheological behavior of the material.

Table 6 Viscosity of candidate materials at selected temperatures and shear rates.

Sample #	Temp (°C)	Viscosity @ 10/s (η)		Viscosity @ 100/s (η)		Shear Thinning
		(Pa s)	% Change	(Pa s)	% Change	% Change
1	230ºC	8,873	-23%	2,124	-26%	-76%
	250ºC	6,858		1,579		-77%
11	270ºC	1,542	-14%	1,002	-32%	-35%
	290ºC	1,332		678		-49%
12	270ºC	2,941	-2%	1,288	-16%	-56%
	290ºC	2,889		1,084		-62%
13	270ºC	2,733	3%	966	-21%	-65%
	290ºC	2,809		760		-73%

The thermal stability of Sample 11 was evaluated as shown in Table 7 below. As expected, the material demonstrated a slight increase in all rheological properties after conditioning at a strain of 0.5% at 1 Hz for a period of 15 minutes. Although a duration of 15 minutes is much longer than expected for BAAM processing, the performance of the material over this time period is indicative of its relative thermal stability. Based on this test, Sample 11 performed well and would be considered "stable" enough for the purposes of BAAM processing, but the effect should be considered when evaluating results of frequency sweep tests which take longer to conduct.

Table 7 Rheological properties as a function of time.

Sample #	**Time (mins)**	**Viscosity (η)**		**Storage Modulus (G')**		**Loss Modulus (G")**	
		(Pa s)	% Change	(Pa)	% Change	(Pa)	% Change
11 (270°C)	0	1,617	30%	3,421	102%	9,565	18%
	15	2,105		6,908		11,281	

The relative bead width consistency of several materials was evaluated with respect to rheological parameters to understand that effect on printability. Attempts were made to create a numerical scoring factor relating the temperature, degree of shear thinning, and viscosity at maximum shear rate to degree of bead thinning, but the resulting values did not directly correlate to a good measure of printability. The exercise did suggest that it may be possible to develop such a printability factor using standard test results after further study and additional test methods. The use of capillary rheology to measure at higher shear rates was suggested to better indicate material behavior in the screw, rather than just as the material is being deposited at the nozzle. Especially for bead width consistency, flow stability through the entire length of the screw and even at the feed throat could be affecting performance. Melt zone movement due to the transient nature of the process could also be a potential cause. The only conclusions that could be made are that detailed simulations of the process may be necessary to fully develop our understanding of the effect of the polymer rheological properties on material printability.

1.2.2.3 Thermo-Mechanical Analysis (TMA)

During the hexagon prints, different amounts of lifting in the corners was observed, particularly for materials that did not have ABS base resin. Due to high fiber alignment in the printing direction (x'), very little warpage occurred in the straightaways, but contraction in the y'-direction through the turns is believed to be the cause of significant lifting in the corners. To better understand these thermal deformations, thermo-mechanical analysis (TMA) was performed on all of the materials from Table 4, as well as filled poly(p-phenylene) ether (PPE) and polycarbonate (PC). Because fiber alignment is considered to be similar in the y'- and z'-directions, and because printing consistently in the y'-direction is difficult, x'- and z'-direction TMA samples were analyzed.

1.3.2.3.1 TMA Procedures

Thermo-Mechanical Analysis (TMA) of BAAM samples was conducted on a Q400 TMA system from TA Instruments. Samples were cut from single-bead printed walls of each of the materials listed in Table 8 below. The TMA sample geometry is a prismatic rectangle measuring 8 mm x 4 mm x 4 mm with the long dimension of the sample oriented along either the direction of the printed bead (x'-direction) or perpendicular the printed layers (z'-direction). The TMA tests were conducted with 0.5 N of restraining force applied to an expansion probe, and the displacement was measured during a temperature change from 35°C to 100°C at a heating rate of 5°C/min.

1.2.2.3.2 TMA Results

The average coefficient of thermal expansion (CTE) for each of the test materials was approximated as linear over the temperature range of interest. Calculated values are included in Table 8 below, and the expansion as a function of temperature for each material is plotted in Appendix B. Inspection of the CTE values in the table shows a drastic difference (5-10x) in the CTE along the x'-direction compared to the CTE across deposited layers (z'-direction). Since reinforcing fibers shear align during the BAAM extrusion process in the direction of extrusion (x'-direction), it is expected that the CTE of the materials would be lower in the direction that is parallel to the long axis of the aligned fibers (x'-direction). In general, one would expect the difference in CTE to increase with increasing reinforcing fiber content as well as the stiffness of the reinforcing fiber (i.e. carbon fiber reinforcement would do more to reduce the CTE than glass fiber). These trends are generally supported by the data below. For example, Sample 15 is a 20% glass fiber composite with an x'-direction CTE of 40 mm/°C, whereas Sample 14 is a 20% carbon fiber composite with an x'-direction CTE of only 21 mm/°C. Additionally, the x'-direction CTE correlates reasonably well with corner lift.

Table 8 Thermo-Mechanical Analysis of BAAM samples.

		Filler 1		**Filler 2**					
Sample #	**Base Resin**	**Type**	**Amount**	**Type**	**Amount**	**Direction**	**Coefficient of Thermal Expansion**		**Corner Lift (in)**
							(µm/m/ºC)	% Change	
1	ABS	CF	20%	-	-	x'	14.3	730%	1/32
						z'	118.7		
3	ABS	CF	20%	-	-	x'	19.5	602%	-
						z'	136.8		
11	PA6	CF	20%	Prop*	25%	x'	14.0	1273%	-
						z'	192.2		
12	PA6	CF	30%	Prop*	20%	x'	20.4	687%	4/32
						z'	160.5		
13	PA66	CF	10%	GF	20%	x'	21.3	761%	3/32
						z'	183.4		
14	PPE	CF	20%	-	-	x'	20.9	406%	4/32
						z'	105.8		
15	PPE	GF	20%	-	-	x'	39.9	290%	-
						z'	155.7		
16	PC	CF	20%	-	-	x'	16.5	475%	3/32
						z'	94.8		

* Prop = Proprietary

1.2.2.4 Further Printability Studies

In order to further investigate printability, a part shape was designed to include a number of features typical of thermoforming or laminating tools and molds (overhangs, bridging, convex and concave surfaces). This shape was printed using CF/ABS (Sample 1) and scanned after cooling to measure the dimensional changes compared to the CAD model. A layer time of 85 seconds was used during the first print, which led to significant sagging in the 45° overhang (Figure 8a). The part was reprinted with 165 second layers, giving much more uniform deviations throughout the overhanging portion (Figure 8b).

Future work will include the printing and scanning of this geometry for several candidate materials. This data will be compared to hexagon lift data and will also be used to calibrate and validate future process simulations and models.

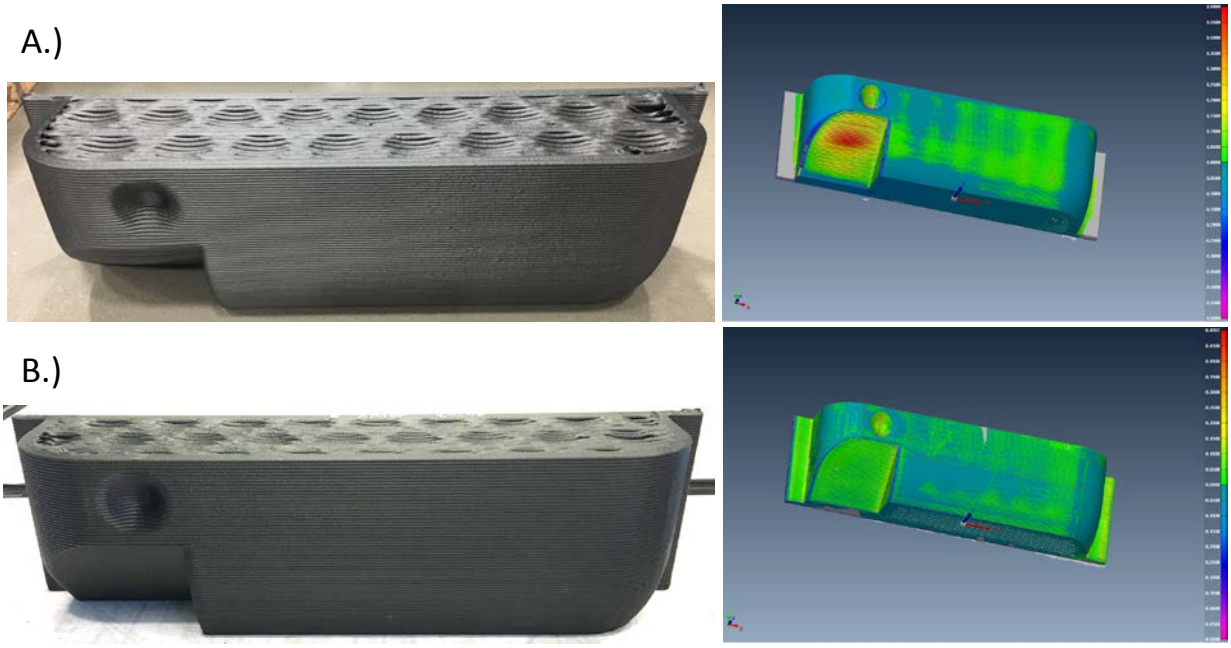

Figure 8. Photograph and laser scan of CF/ ABS tool test print with A) 85 second layer time and B) 165 second layer time. The red region of the 45° overhang section indicates significant sagging due to shorter layer time.

1.2.3 Structural Evaluation

Whereas the preceding section and many previous studies [1,4-7] have largely focused on the mechanical properties of 3D printed materials at both the large and small scales, the current section includes an investigation of affordable manufacturing techniques to reinforce additively manufactured structures, including foam filling, overwrapping with continuous fibers, metal insertion, and 3D printed infill. This work expands upon a previous study of 11 structural sub-elements evaluated under torsional loading [2]; those original boxes were printed with 20% by weight carbon fiber-filled acrylonitrile butadiene styrene (CF/ ABS) (Sample 1, Section 1.3.2) using a laboratory gantry retrofitted with an extruder head [3]. In the current work, the structural sub-element geometry was expanded slightly (914 x 305 x 64 mm^3) in order to accommodate a wider variety of reinforcement techniques (see Table 9), and 30 different types of boxes were printed using the same material on a commercially-available Cincinnati BAAM. These box types were mechanically evaluated under torsional, four-point bending, and shear loading. The results of these tests will be used to communicate design possibilities to automotive designers and will also provide a means to verify FEA models of a wide variety of reinforced additive manufacturing structures.

1.2.3.1 Specimen Fabrication

Boxes were printed in one of two orientations shown in Figure 9. Printer gantry speed was 127 mm/sec and screw speed was 78 rpm for all boxes; this resulted in beads ~7.9 mm wide and 2.54 mm tall after a ~152 mm development region. For the vertically-oriented boxes (Figure 9A), a 152 mm extension was added at the start--these were later removed with a miter saw. For the horizontally-oriented prints (Figure

9B), the outer edge (to be contained within the grips) was printed first in each layer, allowing the full bead width to develop outside of the tested region. In all cases, thermal imaging was used to ensure that the temperature of the layer on which new material was deposited was above the T_g of CF/ ABS (95-110°C). If the temperature drops below the T_g, poor adhesion is expected [3].

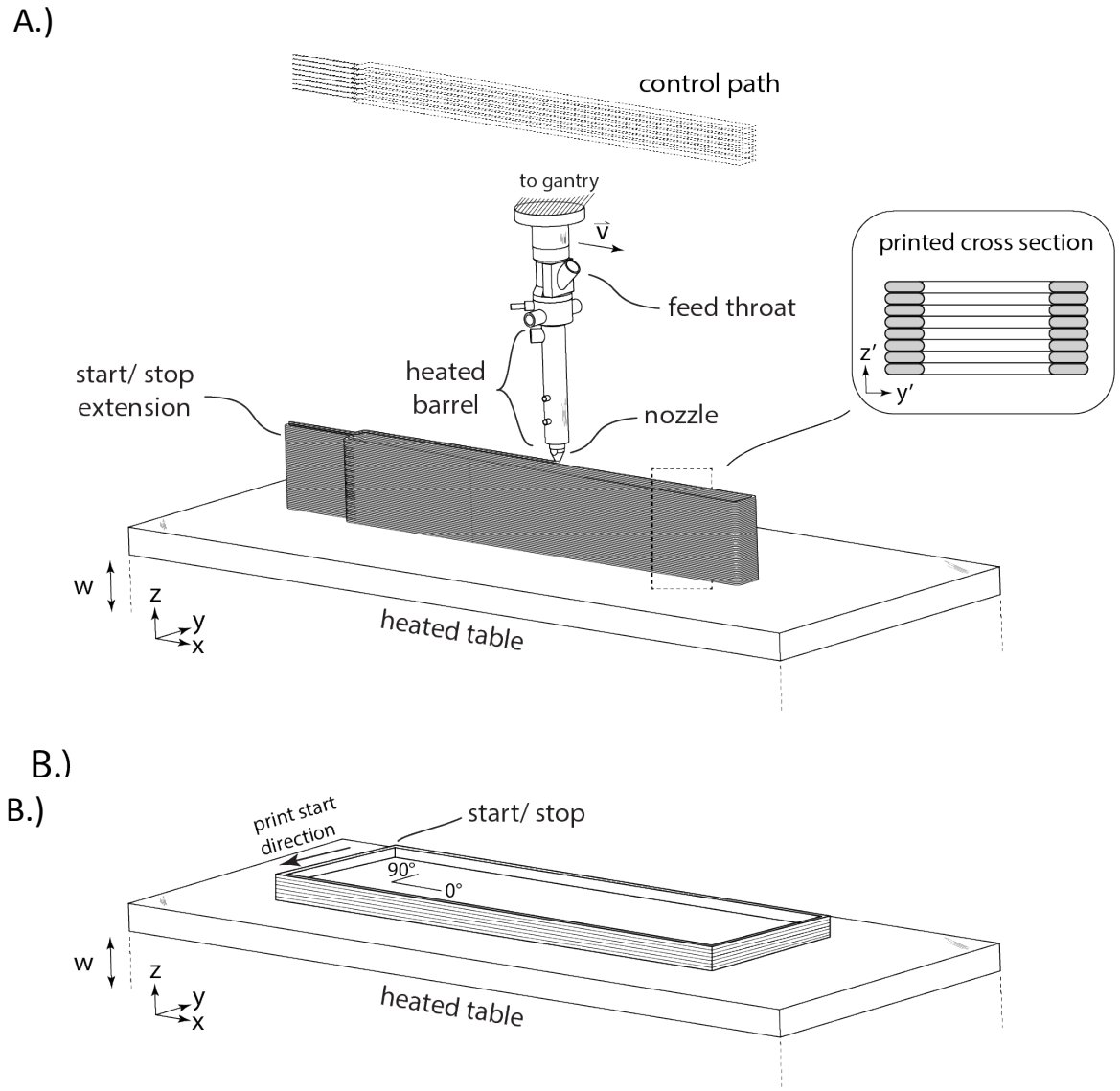

Figure 9. The single wall hollow boxes were printed in the orientations shown: A) vertically-printed box and B) horizontally-printed box. The local coordinate system is given for a cross section (A). The global/box coordinate system is given in (A) and (B). The 0º and 90º lines (B) indicate the direction of solid infill layers relative to the global/box coordinate system x-direction.

Box lids (not pictured) for the vertical parts (Figure 9A) were printed separately in a concentric pattern 3 layers tall such that they were completely solid--overfilled portions were then removed with a planer (DeWALT® DW735 planer with a Byrd Tool® Shelix® cutter head). Box lids were then adhered to the top and bottom of each vertical box using Pliogrip 777 polyurethane adhesive (Ashland Inc.) after preparing all bonding surfaces by sanding with 36 grit abrasive paper using a single action grinder.
Horizontally-printed boxes were printed in two identical parts, one of which is depicted in Figure 9B. The

first three layers were printed solid with an outer perimeter bead and "lines" infill; the infill for each of three layers was either all oriented in the x-direction (0º,0º,0º) or alternating each layer (0º,90º,0º) as shown in Figure 9B. The remaining layers were then printed as single perimeter walls. To obtain the desired 64 mm thickness, a fraction of the top bead of each part was removed with the DeWALT planer. The two parts were then adhered together using Pliogrip 777 after preparing bonding surfaces by sanding with 36 grit abrasive paper using a single action grinder.

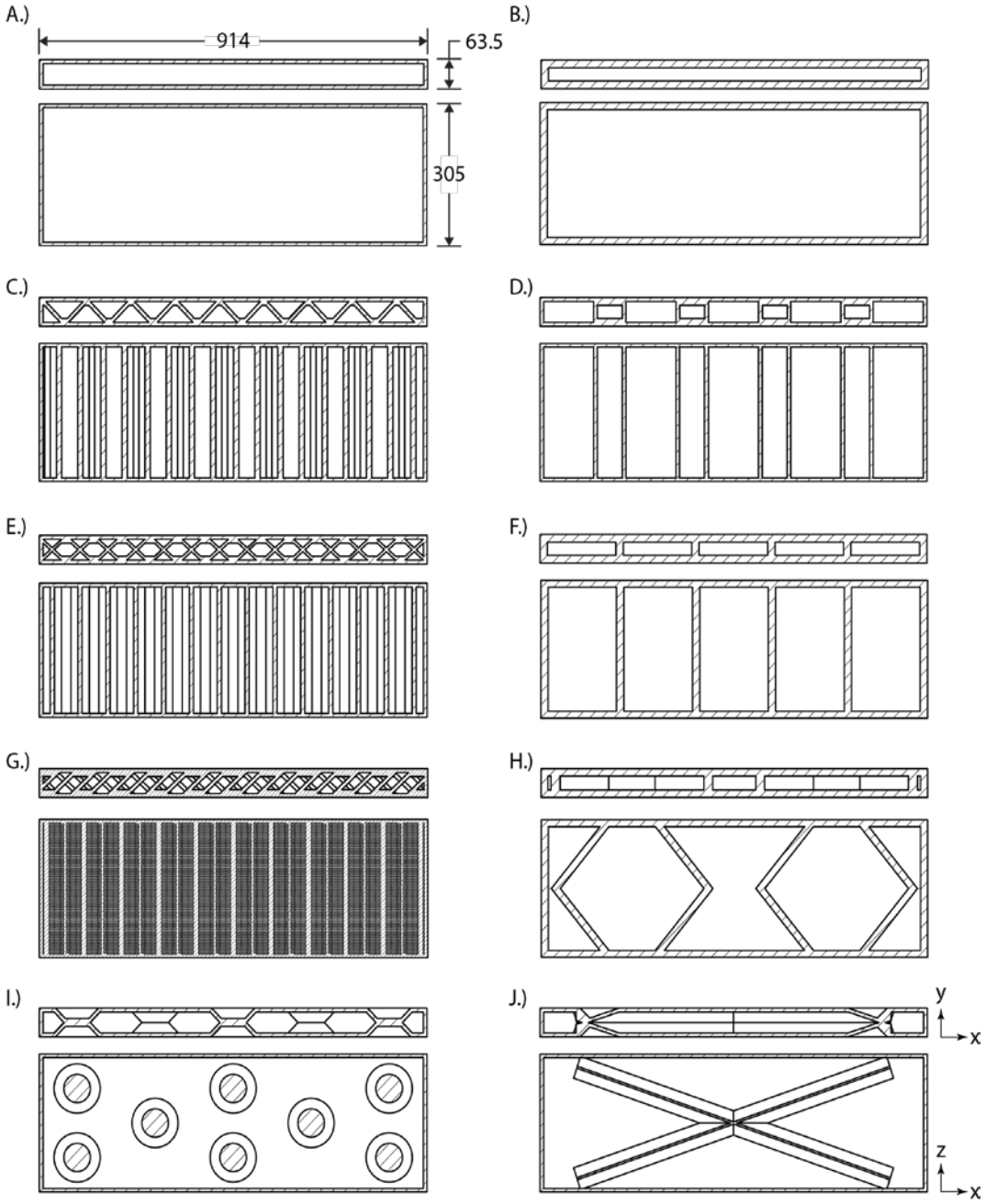

Figure 10. Cutaways through the centerline of sample vertically-printed boxes: A) Single Wall Hollow Control, B) Double Wall Hollow Control, C) W Infill, D) Small Loops Infill, E) Crossed Infill, F) Large Loops Infill, G) Alternating Infill, H) Chevron Loops Infill, I) Spherical Wall Connectors, J) V-ribs Wall Connectors. Global/box coordinate systems are shown in (J).

With the objective of improving upon the specific mechanical performance of the vertically-printed single wall hollow box (Figure 10A), a variety of reinforcement techniques were utilized. Fourteen of the vertically-printed boxes were filled with 2-part polyurethane foams after drilling 25.4 mm diameter holes through the lids. Four of these foam filled boxes were then overwrapped with woven carbon or glass fabric, vacuum-bagged, and infused with Elium® thermoplastic resin (Arkema Inc.). Seven boxes had 3D printed structure/infill that connected the front and back walls of the box using either looped or grid patterns (Figure 10C-H). Two different designs included external walls that connected in the center in some locations (Figure 10I, 10J). Five boxes had a second wall just inside the outer wall, which could then be further reinforced with foam or printed infill--these boxes were given 6-layer tall lids in order to maintain outer wall thickness for the entire box (Figure 10B, 10D, 10F, 10H).

For comparison with the vertically-printed single wall hollow box (Figure 10A), two single wall hollow boxes were printed horizontally; one had all three solid infill layers printed in the x-direction (0º,0º,0º), whereas the other had alternating solid infill layers (0º,90º,0º). A third variation of this box was printed with diagonal solid infill layers (45º,0º,-45º), but it warped significantly after cooling such that assembly was impossible. One of the horizontal boxes (0º,90º,0º) included 46 mm thick inlaid Plascore® PCGA-XR2 3003 commercial grade aluminum honeycomb with 12.7 mm cell size that filled the entire cavity and was adhered to the printed parts by Pliogrip 777. Another horizontal box (0º,90º,0º) included two diagonally-printed (12.2º relative to the x-direction) sleeves for 25.4 mm square steel tubes 825 mm long that were inserted and adhered using Pliogrip 777. Finally, in order to relieve the stress concentrations in the horizontally-printed boxes where the solid layers met the single wall layers, a stepwise internal radius was created in one box: three layers were printed solid (0º,90º,0º), followed by two layers of three concentric perimeter beads, followed by two layers of two concentric perimeter beads, followed by the remaining single wall perimeter layers.

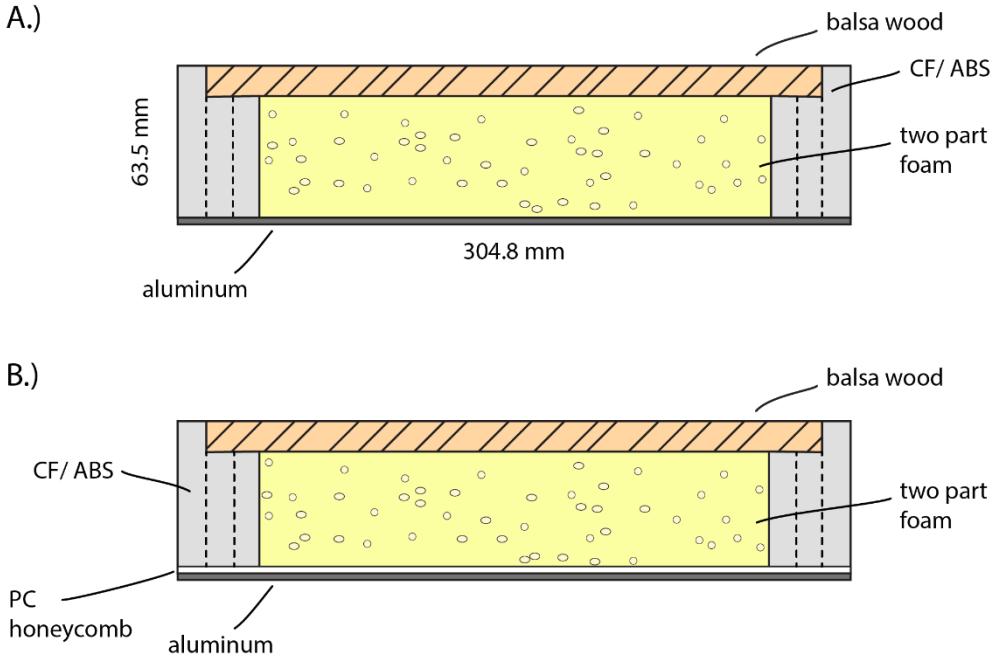

Figure 11. Cross sections of the two Balsa and Aluminum box types: A) aluminum sheet adhered to the bottom and B) aluminum sheet adhered to PC honeycomb and then printed over.

For comparison to traditional manufacturing methods, two boxes were constructed by welding aluminum sheet metal (2.03 mm thick), one of which was then filled with foam. An additional box type combined

additive manufacturing and traditional manufacturing techniques (Figure 11). A balsa wood top panel was adhered to a horizontally-printed CF/ ABS frame using Pliogrip 777. In one variation, the 2.03 mm thick aluminum bottom sheet was adhered to the printed frame using Pliogrip 777 (Figure 11A); in the other version, a 3.18 mm thick Plascore® PC2 polycarbonate (PC) honeycomb with 6.35 mm cell size was adhered to the 2.03 mm thick aluminum sheet using Plascore® P206 epoxy adhesive by the manufacturer, and then the CF/ ABS frame was printed directly on top of this honeycomb surface (Figure 11B).

After assembly, all boxes to be tested in shear were planed with the DeWALT planer in order to remove the bead cusps on the front and back surfaces; aluminum shear plates were then bonded to these faces using Henkel LOCTITE® H3300 adhesive after surface preparation by light abrasive sanding with 80 grit pads. In order to perform Digital Image Correlation (DIC), all boxes were given a speckle coating prior to testing using Homax Orange Peel Wall Texture.

1.2.3.2 Structural Test Methods and Procedures

Structural sub-elements were tested in four-point bending, torsion, and shear using the apparatus in Figure 12; this structure is much more rigid than the torsion rig used in [2]. The steel four-point bend supports are 38 mm in diameter, the support span is 838 mm, and the load span is 279 mm (Figure 12B). The torsion grips are 864 mm apart and consist of 38 mm diameter grip faces that clamp onto the specimen using hand tightened vice fixtures (Figure 12C). Central shear plates are 152 mm wide, and the distance between central and outer shear plates is 305 mm (Figure 12D). A complete CAD model of this test rig is available at OnShape.

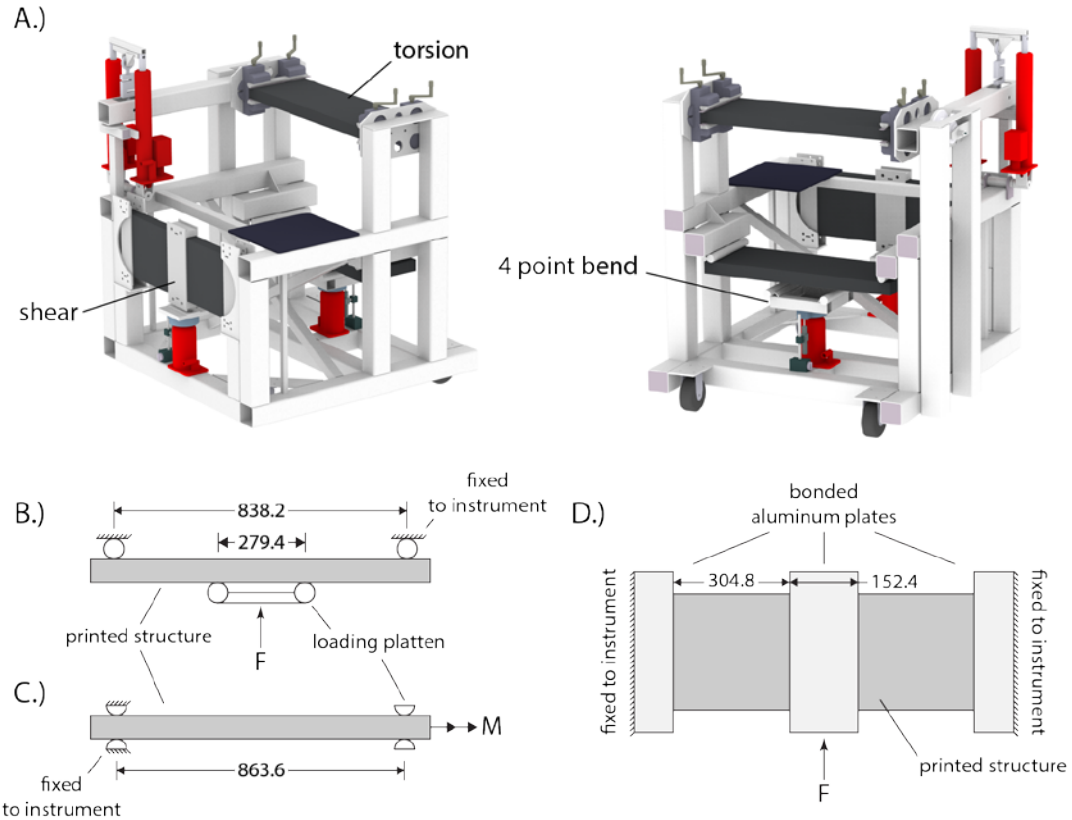

Figure 12. A) Front and back views of structural test apparatus with bending, torsion, and shear capability, along with 2D schematics of B) bending, C) torsion, and D) shear.

All loads were applied by manually actuating hydraulic jacks. Displacements were measured using an LVDT for bending and shear, and a rotary encoder for torsion. Loads were measured using canister-type load cells for bending (66.7 kN, +/-0.02 kN) and shear (222 kN, +/-0.07 kN); whereas an S-type load cell (44.4 kN, +/-0.01 kN) on a 0.76 m long lever arm was used for torsion. All data signals were acquired using a National Instruments data acquisition system and LabVIEW software.

In addition, full field surface displacements were recorded using 3D DIC with Vic-3D™ software. Two cameras were mounted in stereo in order to view the top surface of all bending and torsion boxes, whereas a single camera was used to view one side of the shear specimens for 2D DIC. All images were collected at 2 Hz. A sample comparison of surface displacements obtained in this fashion compared to a structural simulation of four-point bending is given in this work; future work will include the comparison of all tested boxes to finite element analysis (FEA) in order to validate the accuracy of the additive manufacturing structural model.

1.2.3.3 Structural Test Results

The bending, torsion, and shear results are listed in Table 9 as a function of box weight. Note that the shear box specific stiffness was calculated using the bending box weight. Fabric reinforced structural elements exhibited progressive failure modes as compared to boxes that were only printed, which failed more abruptly. None of the vertically-printed boxes failed at the adhesive bond line, indicating good adhesive selection for the application and acceptable load transfer between the bonded parts. Both of the carbon-overwrapped boxes failed within the grips; this is likely due to the stress concentration where the overwrapped faces met the uncovered faces on the ends. While the body primer used in several of the vertically-printed foam filled boxes adhered well to the printed material, several failures initiated within this layer, suggesting that it has unacceptably low shear strength for this application.

The horizontally-printed boxes had more stress concentrations by design and also carried high stresses across adhesive layers; thus, these boxes consistently had lower specific strength than the vertically-printed boxes. The hollow horizontally-printed boxes failed at the stress concentration where the solid layers met the single wall layers, as well as along the adhesive centerline. The internal radius horizontally-printed box failed similarly at the stress concentration between the single wall and double wall layers and then migrated to the adhesive centerline. The adhesive failed between the aluminum honeycomb and the printed box, and in both types of balsa boxes, the adhesive layer bonded to the aluminum sheet failed (either the aluminum/printed frame adhesive layer or the aluminum/PC honeycomb adhesive layer).

In Figure 13, bending stiffness and strength have been normalized by the weight of each box, and ovals have been drawn to approximate the bounds for each family of reinforcement. The aluminum family exhibited the highest specific bending stiffness, whereas the overwrap family displayed the highest specific strength. Grid infill also consistently outperformed both the single wall (#1) and double wall (#14) hollow control boxes, as did the majority of the external printed connectors (with the exception of #23, the spherical wall connectors box).

In the same fashion, the torsion results have been compiled in Figure 14. Again, the aluminum boxes exhibited superior specific stiffness; however, this difference between the aluminum and the printed structural sub-elements is much greater in torsion than in bending. For this reason, the data has also been rescaled to exclude the aluminum boxes in Figure 14. As in bending, the overwrap family was stiffer and stronger by weight than both hollow control boxes (#1 and #14). The balsa boxes were stronger and had similar stiffness compared to the single wall hollow box (#1). Although many of the other reinforced boxes demonstrated improved specific strength compared to the single wall hollow box (#1), only the horizontally-printed boxes were as stiff. Note also that #23, the spherical wall connectors box, performed significantly better under torsional loading than the V-rib boxes.

Table 9 Bending, torsion, and shear results.

			BENDING			*TORSION*			*SHEAR*
#	**Description**	**# of walls**	**Weight (kg)**	**Stiffness/ Weight ($kN \cdot m^{-1} \cdot kg^{-1}$)**	**Specific Ultimate Load ($kN \cdot kg^{-1}$)**	**Weight (kg)**	**Specific Stiffness ($N \cdot m \cdot rad^{-1} \cdot kg^{-1}$)**	**Specific Ultimate Torque ($N \cdot m \cdot kg^{-1}$)**	**Specific Stiffness ($kN \cdot m^{-1} \cdot kg^{-1}$)**
1	Hollow Control	1	5.94	314	4.45	5.99	2244	386	2426
2	32 kg/m^3 USC [a]	1	6.46	311	4.19	6.44	2047	488	2146
3	128 kg/m^3 USC [a]	1	8.10	267	4.01	8.44	1754	520	1831
4	32 kg/m^3 DB [b]	1	6.51	304	3.43	6.51	2067	335	-
5	112 kg/m^3 DB [b]	1	8.01	345	5.11	7.98	1847	418	-
6	384 kg/m^3 DB [b]	1	13.20	168	1.61	13.06	1378	294	-
7	Primer, 384 kg/m^3 DB [b]	1	13.45	298	2.18	13.40	1337	256	-
8	2-ply CF/EO, 32 kg/m^3 USC [ac]	1	7.19	389	6.80	7.17	2416	709	2195
9	4-ply CF/EO, 32 kg/m^3 USC [ac]	1	7.76	433	7.06	7.82	2461	687	2095
10	2-ply FM/EO, 32 kg/m^3 USC [ad]	1	7.64	362	7.85	7.82	3185	879	2238
11	W Infill	1	8.87	472	6.36	8.71	1662	463	1620
12	Crossed Infill	1	11.84	395	6.36	11.66	1488	465	1498
13	Alternating Infill	1	12.63	369	6.47	12.63	1435	357	1423
14	Hollow Control	2	10.75	293	4.50	10.80	1851	416	1915
15	32 kg/m^3 USC [a]	2	11.32	303	4.85	11.36	1775	418	1639
16	W Infill	2	12.86	438	6.85	12.90	1719	541	1722
17	Small Loops Infill	1	8.44	322	4.16	8.41	1682	373	1759
18	Large Loops Infill	2	11.32	233	3.10	11.29	1752	448	1734
19	Chevron Loops Infill	2	11.48	300	4.98	11.50	1582	484	1690
20	V-ribs WC [e]	1	6.08	344	5.40	6.08	993	169	1247
21	V-ribs WC, 32 kg/m^3 USC [ae]	1	6.71	354	5.38	6.65	916	160	1217
22	V-ribs WC, 2-ply CF/EO, 32 kg/m^3 USC [ace]	1	7.62	484	5.70	7.62	1214	299	-
23	Spherical WC, 32 kg/m^3 USC [ae]	1	6.99	243	3.28	6.69	1471	434	1600
24	Horizontal 0,0,0	1	5.67	329	2.43	5.65	2872	222	3272
25	Horizontal 0,90,0	1	5.67	272	1.57	5.65	2685	264	3178
26	Horizontal 0,90,0 Internal Radius	1	6.21	298	2.39	6.33	2267	205	2774
27	Horizontal 0,90,0, 25.4 mm Steel Tube Insert	1	9.62	270	2.91	9.55	2142	245	-
28	Horizontal 0,90,0, Honeycomb Insert	1	6.76	454	4.22	6.78	2864	370	-
29	Balsa and Al Sheets, 32 kg/m^3 USC [a]	1	6.46	372	6.43	6.46	2140	642	-
30	Balsa and PC/Al Sheets, 32 kg/m^3 USC [a]	1	6.69	389	6.31	6.67	2295	598	-
31	2.03 mm Al box (not printed)	N/A	3.74	525	4.86	3.74	10182	705	7103
32	2.03 mm Al box (not printed), 32 kg/m^3 USC [a]	N/A	4.45	724	5.42	4.40	10555	897	6582

[a] USC = US Composites Foam-Filled
[b] DB = Dow Betafoam Foam-Filled
[c] CF/EO = Carbon Fabric/ Elium Overwrap
[d] FM/EO = Fiberglass Mat/ Elium Overwrap
[e] WC = Wall Connectors

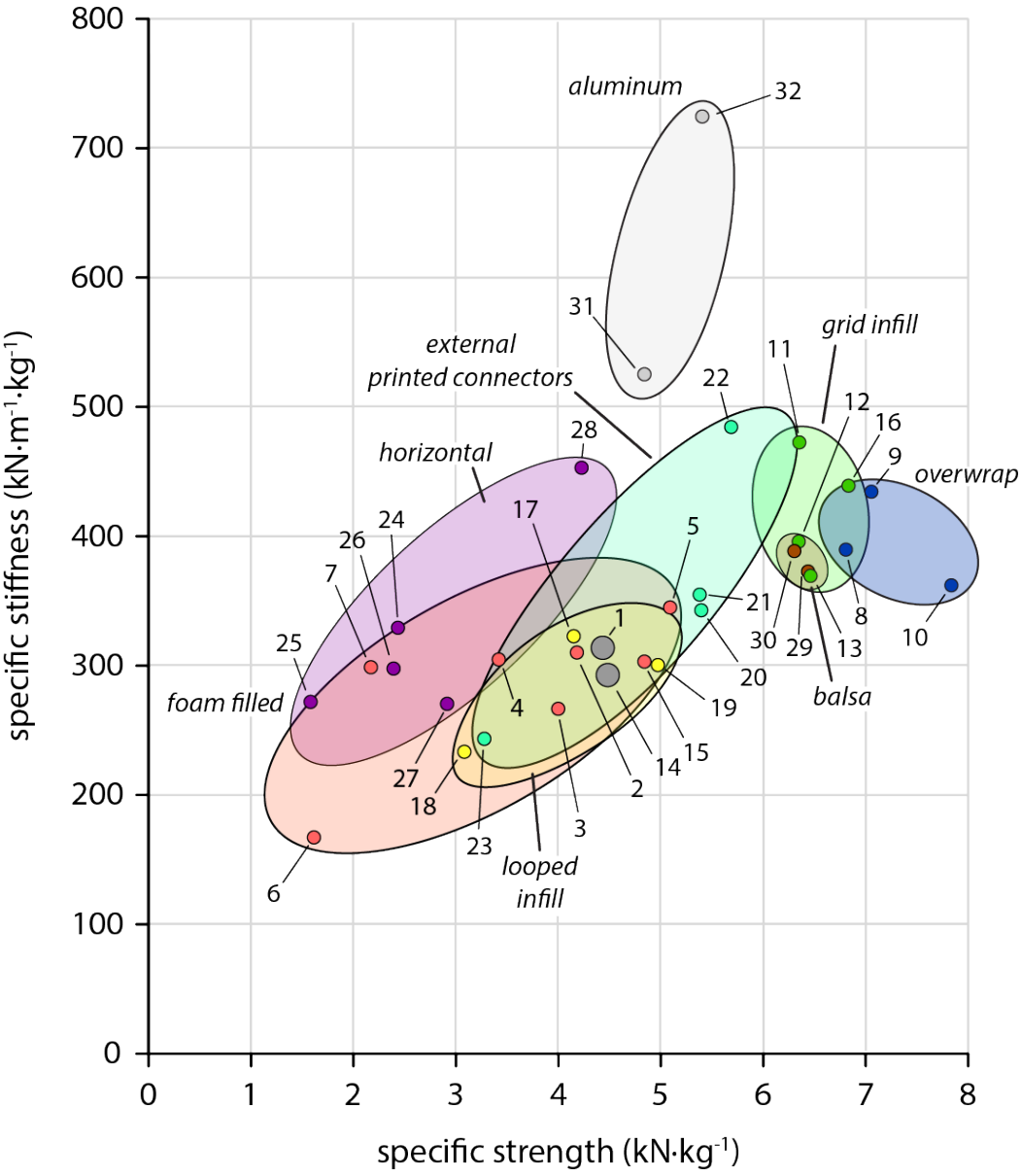

Figure 13. A comparison of specific bending stiffness versus specific ultimate strength illustrates the effectiveness of the various reinforcement and construction methodologies used with additive manufactured structures. Many of the reinforcement methodologies improved the specific performance of the control structure in bending.

The vast superiority of the aluminum boxes in terms of specific torsional stiffness is attributed to the high fiber alignment in the direction of printing of the additively manufactured boxes. These aligned fibers contribute significantly to the bending stiffness (σ_{xx}) (relative to the global/box coordinate system), but because they do not cross the bead interface, they do little to improve torsional stiffness (γ_{xz}) of the base resin. Although shear properties were not reported, the high degree of anisotropy (~4x) of this printed material has been demonstrated in terms of print-direction (x') and stack-direction (z') tensile stiffness [2].

Especially in torsion, the 2-ply glass fiber overwrapped box (#10) performed much better than the 2-ply carbon fiber overwrapped box (#8). This unexpected result is most likely due to incompatibility between the infused thermoplastic resin and the carbon fiber sizing. It is therefore reasonable to infer that proper interaction between resin and fiber would cause the carbon fiber overwrapped boxes to have superior performance in terms of both specific stiffness and strength compared to all other printed structural sub-elements.

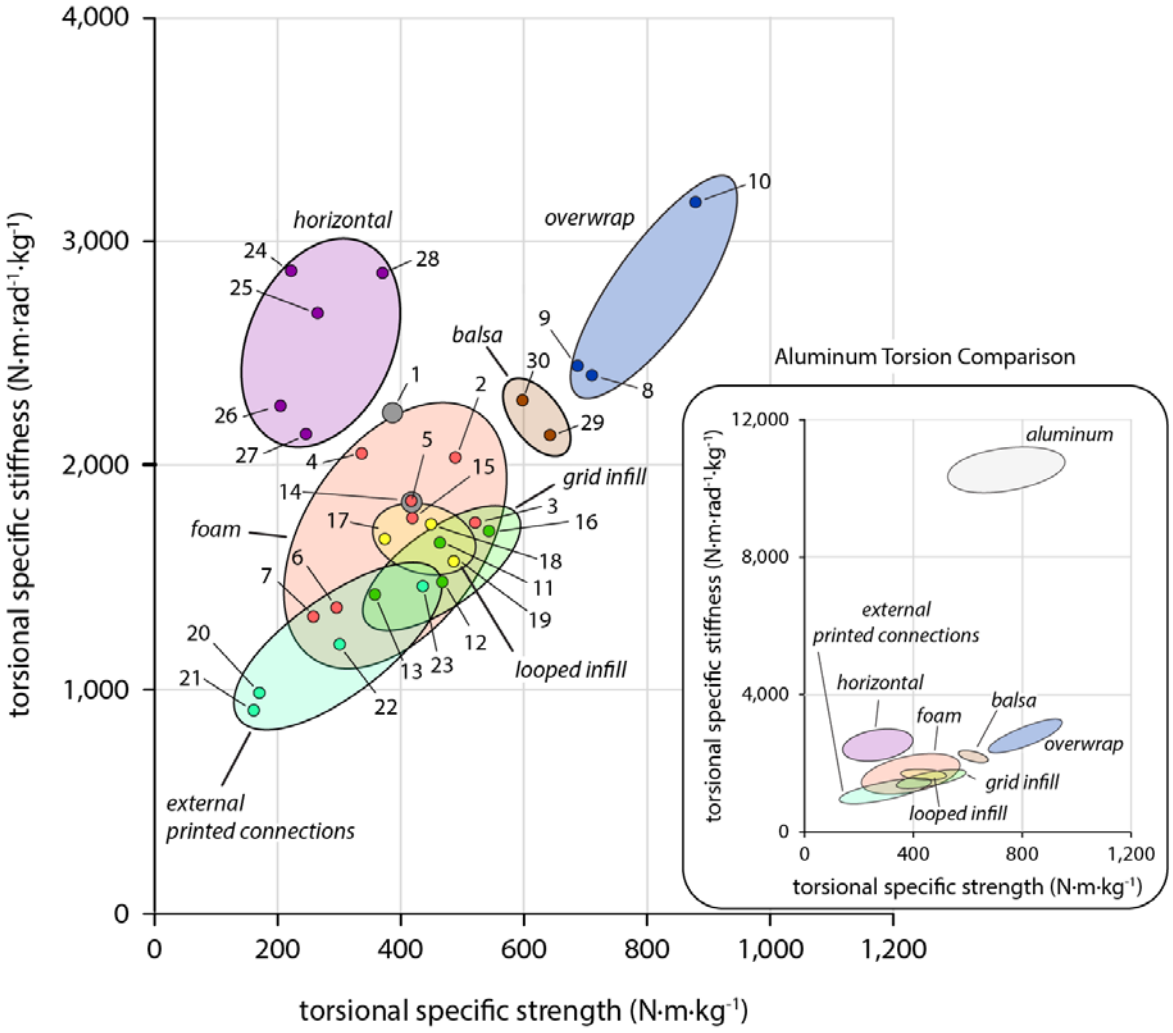

Figure 14. Performance in torsion appears to be highly sensitive to interlaminar properties with most reinforcement techniques resulting in a weight increase without a commensurate gain in specific stiffness or strength; the exception to which was external composite reinforcement (overwrap).

Due to the high loads necessary to fail the shear boxes (198 kN for the double wall hollow box #14), most of these boxes were not loaded to failure; instead they were unloaded at approximately 110 kN. For this reason, only specific shear stiffness has been reported for the shear samples; specific shear stiffness was calculated using the weight of the corresponding bending box due to the material removed during planing. Figure 15A compares the specific shear stiffness and specific bending stiffness for each box using two different y-axes. Similarly, Figure 15B compares the specific shear stiffness to the specific torsional

stiffness. The shear boxes trend much closer with torsion than with bending because both of these loading cases (Figure 15B) are dominated by shear stress (γ_{xz}). However, it is important to note that the shear boxes also experience significant σ_{xx} bending loads; this explains why the printed shear boxes performed closer to the isotropic aluminum boxes than the torsion boxes in terms of specific stiffness.

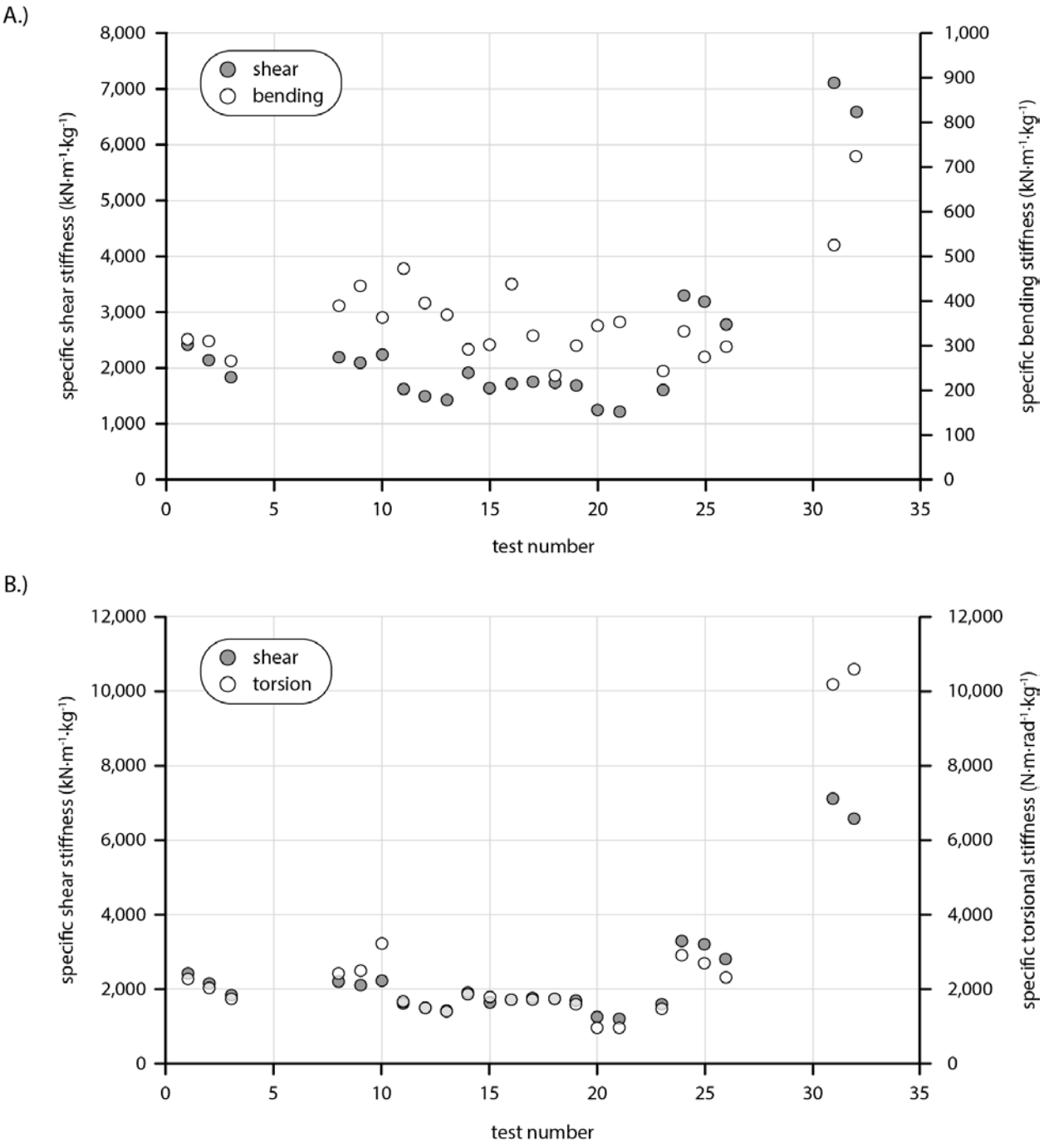

Figure 15. A) Relative comparison of shear and bending specific stiffness. B) Relative comparison of shear and torsion specific stiffness.

Figure 16A shows the specific bending performance of the single wall hollow boxes (Figure 10A) and the V-rib boxes (Figure 10J). The addition of foam to each hollow box caused little change in the specific performance; however, the addition of overwrapped carbon fiber caused a significant improvement in specific stiffness for the V-rib box, as well as significant improvements in both specific stiffness and strength for the single wall hollow box. The V-rib boxes demonstrated higher specific stiffness than each corresponding single wall hollow box.

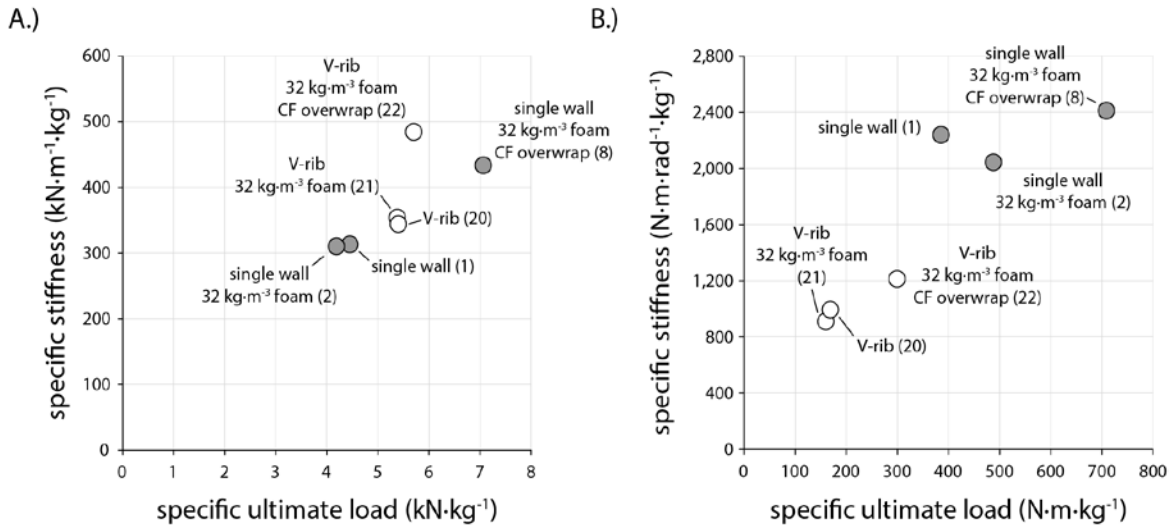

Figure 16. Effect of adding foam and overwrap to the single wall hollow (grey) and V-rib (white) boxes: A) Bending and B) Torsion.

Figure 16B shows the specific torsional performance of the single wall boxes and the V-rib boxes. Foam did not cause much change in the specific mechanical performance, but the addition of carbon fiber overwrap caused improvements in both specific strength and specific stiffness for both box types. Unlike in bending, the single wall hollow boxes performed much better than the V-rib boxes in torsion.

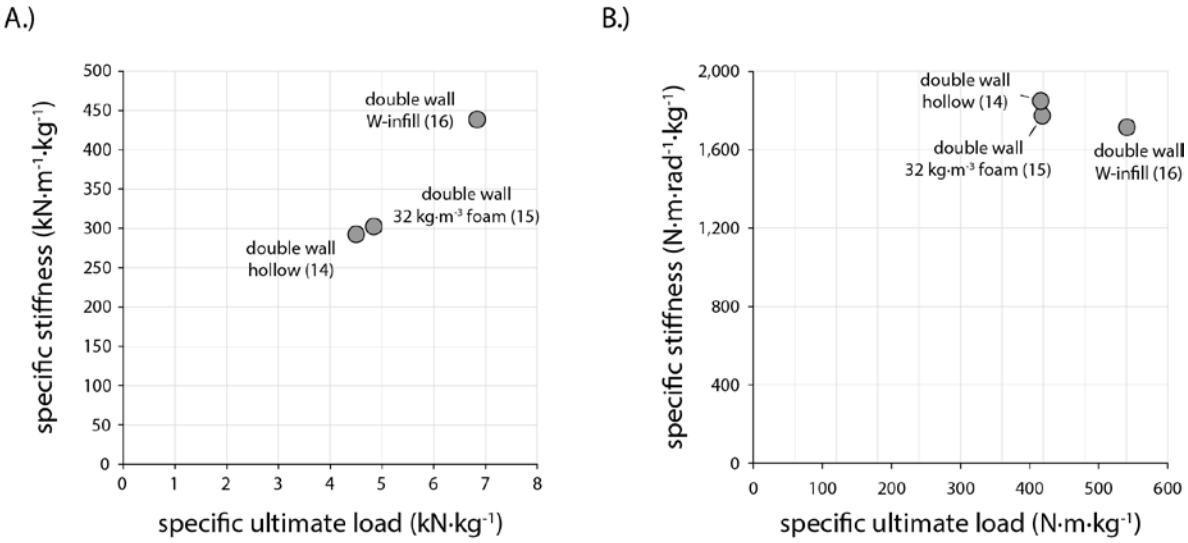

Figure 17. Effect of adding foam or infill to the double wall hollow box: A) Bending and B) Torsion.

Figure 17A displays the effects of adding infill or foam to the double wall hollow box (Figure 10B) in bending. Whereas foam caused minor structural improvements, infill caused ~50% improvement in both specific stiffness and specific strength.

Figure 17B shows the effects of adding infill and foam to the double wall hollow box under torsional loading. Whereas foam caused no change in specific strength and a minor reduction in specific stiffness, infill caused a 50% increase in specific strength and a 10% reduction in specific stiffness.

Figure 18A gives the bending results for several different types of looped infill designs that connect the front and back walls (Figure 10D, 10F, 10H) compared to the double wall hollow box (Figure 10B). The small loops box performed best in terms of specific stiffness, whereas the chevron loops box performed best in terms of specific strength. The large loops box performed much worse than the double wall hollow box in terms of both specific stiffness and specific strength.

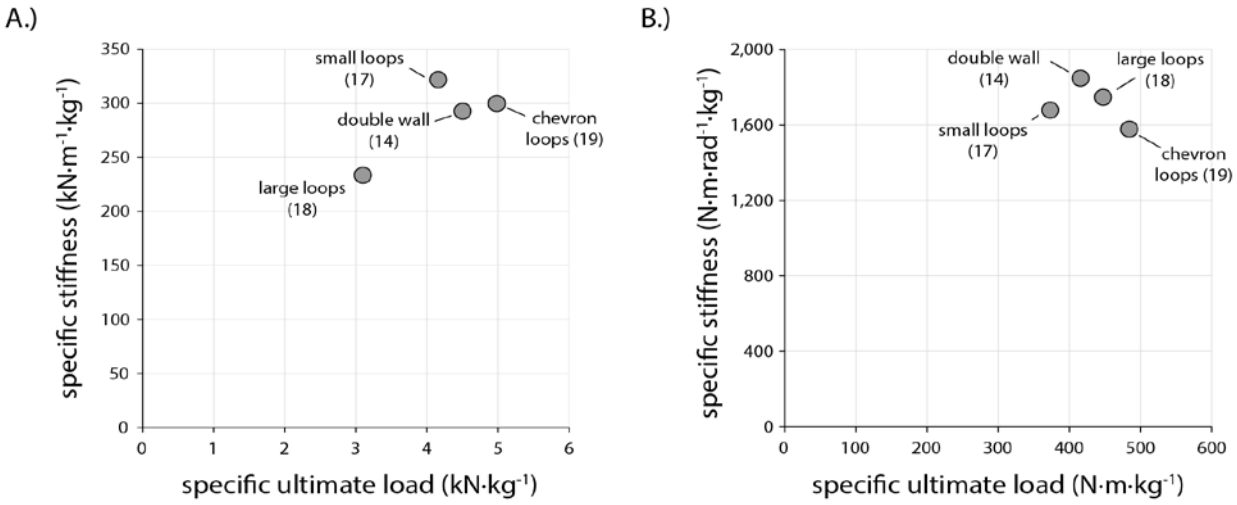

Figure 18. Effect of different types of looped infill compared to the double wall hollow box: A) Bending and B) Torsion.

Figure 18B displays the torsional results for several different types of looped infill designs that connect the front and back walls compared to the double wall hollow box. The double wall hollow box performed best in terms of specific stiffness, whereas the chevron loops box performed best in terms of specific strength. Unlike in bending, the large loops box performed better than the small loops box in both specific stiffness and strength under torsional loading.

1.2.3.4 Digital Image Correlation

The experimental results of the structural testing contain about 200GB of data from the digital image correlation (DIC) system. This is currently contained as an archive of raw data and processed files within Local Motors file servers. It is expected that the data will be published once an optimum outlet is identified. For the purposes of this report, surface strain maps (ε_{xy}) were prepared for the complete set of structural sub-elements for a single load (bending, torsion, and shear) and provided in Appendix C.

1.2.3.5 Structural Simulations

One of the main objectives of this test program is to provide data for validation of FEA models of different

sub-element types so that designers may have confidence in structural models of future vehicle designs. Because the BAAM process is new, and the material architecture varies from traditional laminate composites, the development of efficient structural models is necessary. One approach is to derive a mesh from the machine G-code that contains the print orientation at each node [1]. This approach will provide

the most accurate representation of the orthotropic properties of 3D printed material but results in very large mesh sizes and computationally intensive models.

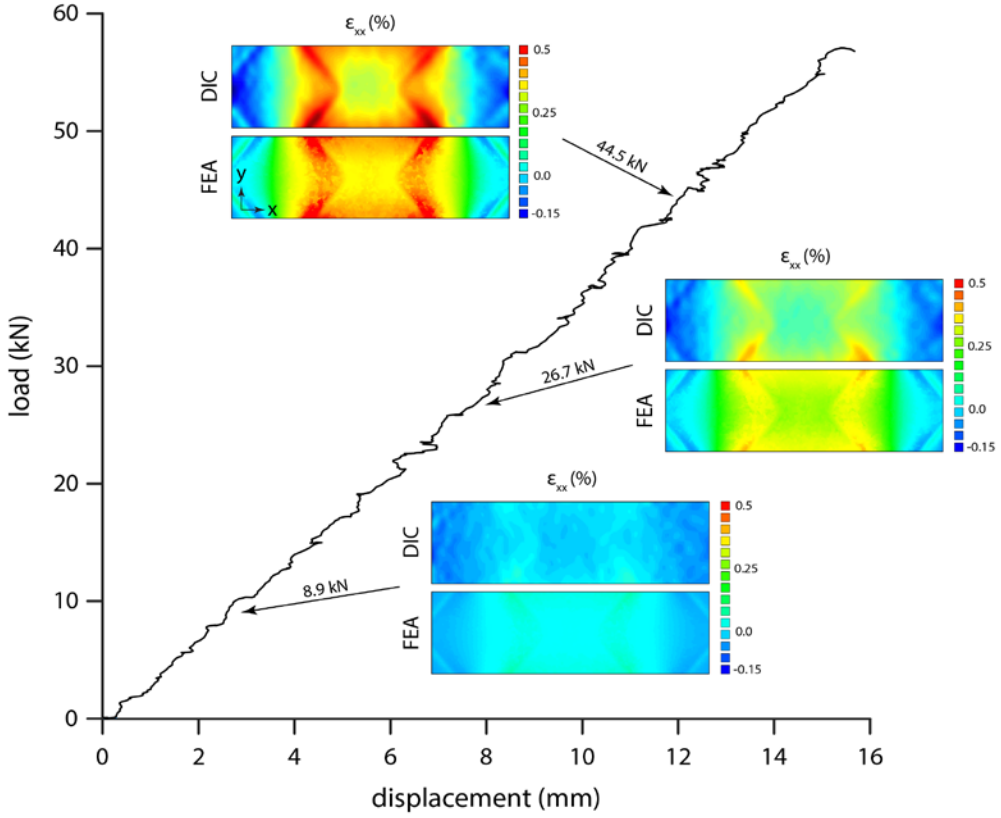

Figure 19. Four Point Bend FEA and DIC Comparison of Chevron Loops Infill box.

At this stage, a more simplistic approach has been taken for existing designs that assumes x'-direction (print direction) properties in-plane and z'-direction (vertical direction) properties in the stacking direction. For many designs that do not have extensive y'-direction dimensions, this may be an acceptable approximation that significantly reduces the complexity of the FEA modeling process. Figure 19 shows a comparison between DIC test results and FEA predictions for the four point bending of the chevron loops infill box (Figure 10H). The surface strains in the x'-direction are shown for the entire tensile surface of the specimen at loads of 8.9, 26.7, and 44.5 kN. Good agreement was observed between the measured x-direction surface strains, from 3D DIC, and those obtained through FEA modeling. This is evident in the color maps of Figure 19 where the strain values are scaled the same.

1.3 BENEFITS ASSESSMENT

The impact of this work is already being seen in the development of the 3D printed Olli concept vehicle. This design was selected as a finalist in the Awards for Composite Excellence at the CAMX event. As

shown in Figure 20, the primary structure consists of two primary components, the upper and lower chassis, that are entirely produced by additive manufacturing. The four corner structures are molded composite laminate, whereas the four pillars and structural hand rails are extruded aluminum tubing. Further development of the design into a commercial product is being undertaken, and it is expected to go into production.

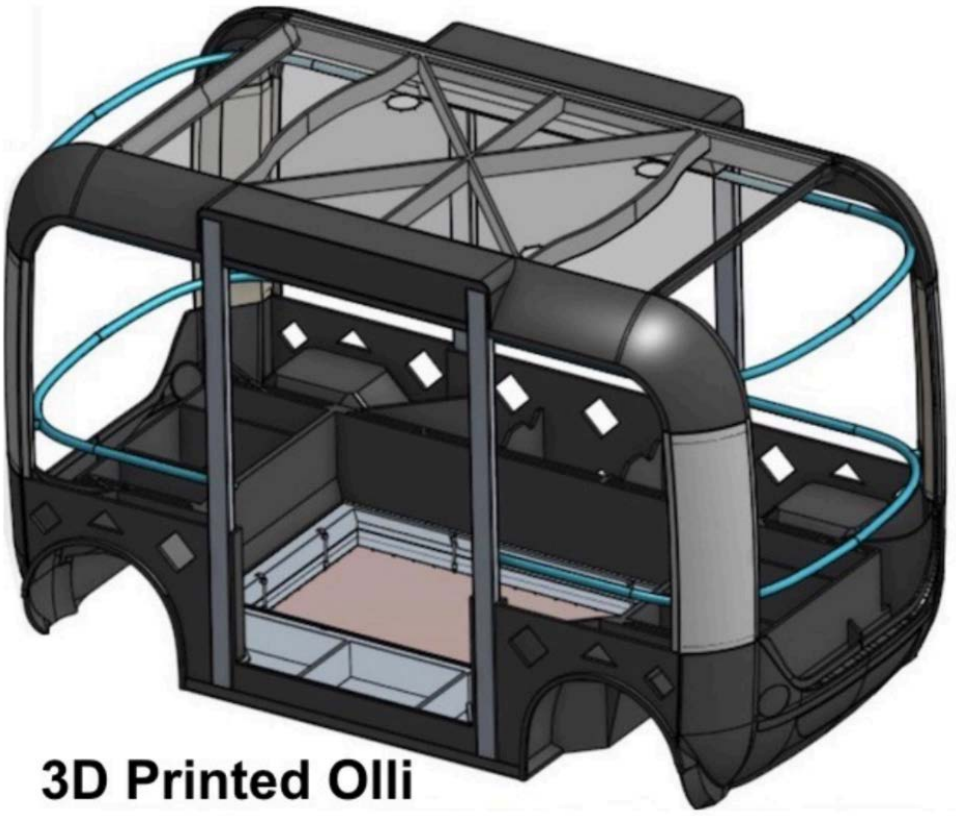

Figure 20. 3D Printed Olli Design and Concept Vehicle

1.3.1 Commercialization

Local Motors' vision is to build new micro-factories in many major cities that will each produce up to 250 advanced self-driving electric vehicles per year and create approximately 75-125 skilled jobs at each location. On-site workforce training and internship programs will also be implemented at each facility. The self-driving shuttle vehicles branded as "Olli" have demonstrated a significant number of pilot program sales. They provide a transportation solution that is ideal for use in first mile and last mile transit.

The company growth strategy includes establishing microfactories in major cities to produce vehicles tailored to local markets and current trends. The microfactory approach enables scalable expansion in concert with demonstrated demand. The advanced manufacturing processes enable customer configuration and on-demand build capability, which are predicted to improve profitability over traditional mass manufacturing.

1.4 CONCLUSIONS

A significant number of new materials were evaluated with the BAAM system, and a deep understanding of printability characteristics was developed. Mechanical properties were established at a screening level through tension tests in the print and stacking directions. Rheological behavior was evaluated and related to printability for a number of compounds. Both the complex viscosity over a range of shear rates and the degree of shear thinning were considered to affect printability. The thermo-mechanical behavior was evaluated in both the print and stacking directions, and this was compared to the dimensional stability of large printed structures. A sample tool shape was printed and dimensionally scanned to compare as-printed dimensions to the design dimensions; this data is expected to be valuable in the validation of process simulations. The collection of all this data and the experience of printing with the wide variety of materials has contributed to the understanding of printability and will lead to more rapid development of specialized materials for a variety of applications.

Structural evaluations of complex printed parts and those reinforced with advanced composites has generated a very large data set that will be utilized in future work to calibrate and verify structural models and enable efficient designs. Comparisons of the groups of structure types in terms of specific stiffness and strength allows the selection of those with the highest structural performance per unit mass. This should aid the design of vehicle structures for the additive process and show the possibilities for utilization of large scale extrusion deposition in the primary structure of production vehicles. Although the work was primarily experimental, some simple FEA models were prepared and compared to the experimental results with good correlation; this suggests that the data is valuable for the planned future work to simulate the sub-component structures and develop test verified models that may be used to quickly design efficient vehicle structures.

1.5 RECOMMENDATIONS

An enterprise level IACMI project was proposed to continue and expand this work. The project includes a materials development effort, a simulation effort, and machine development to further the state of the art of this process and the quality of products that may be achieved through its implementation. It is recommended that this second phase be approved so that this valuable work may be continued and improved upon.

2. LEAD PARTNER BACKGROUND

Local Motors is a technology company that designs, builds, and sells vehicles. They partnered with ORNL and Cincinnati, Inc. to produce the world's first 3D printed car live at the International Manufacturing Trade Show (IMTS) in 2014 and have continued to develop the technology necessary to produce vehicles by additive manufacturing. They have established a team of materials engineers including Robert Bedsole, Charles Hill, and Kyle Rowe, who have been working since early 2015 to develop new materials for the application, better understand the process, and characterize the structural performance of complex printed shapes. Local Motors innovates through co-creation and micro-manufacturing to bring vehicles to market at unprecedented speed.

3. REFERENCES

1. Talagani, M. R., et al, "Numerical Simulation of Big Area Additive Manufacturing (3D Printing) of a Full Size Car.", *SAMPE Journal*, 51(4), (July/Aug 2015): 27-36.
2. Hill, C. S. et al, "Materials and Process Development for Direct Digital Manufacturing of Vehicles," *SAMPE Conference Proceedings.* Long Beach, CA, May 23-26, 2016. Society for the Advancement of Material and Process Engineering.
3. Dinwiddie, R.B., et al, "Infrared Imaging of the Polymer 3D-Printing Process." *Proceedings of SPIE Volume 9105. Thermosense: Thermal Infrared Applications XXXVI.* San Diego, California, August 17-21, 2014. Ed. Colbert F.P., and Hsieh, S.
4. Duty, C., Drye, T., Franc, A. "Material Development for Tooling Applications Using Big Area Additive Manufacturing (BAAM)." *ORNL Manufacturing Demonstration Facility Technical Collaboration Final Report*. MDF-TC-2014-053, 2015.
5. Love, L., et al, "Breaking Barriers in Polymer Additive Manufacturing." *SAMPE Conference Proceedings.* Baltimore, MD, May 18-21, 2015. Society for the Advancement of Material and Process Engineering.
6. Love, L., et al, "The Importance of Carbon Fiber to Polymer Additive Manufacturing.", *J. Mater. Res.*, 29(17) (2014): 1893-1898.
7. Tekinalp, H. L., et al, "Highly oriented carbon fiber–polymer composites via additive manufacturing", *Comp. Sci. Tech.* 105 (Oct 2014): 144-150.

APPENDIX A: Rheology

A.1 Sample 1: 20% CF/ ABS

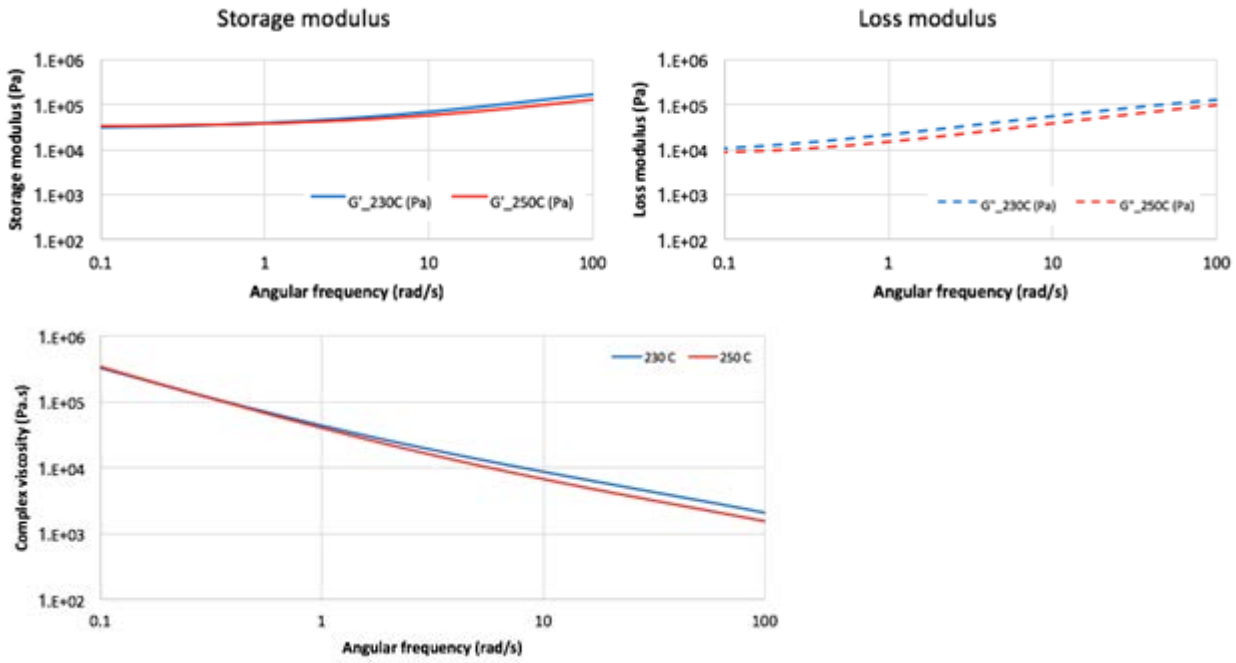

A.2 Sample 11: 20% CF/ 25% Proprietary/ PA6

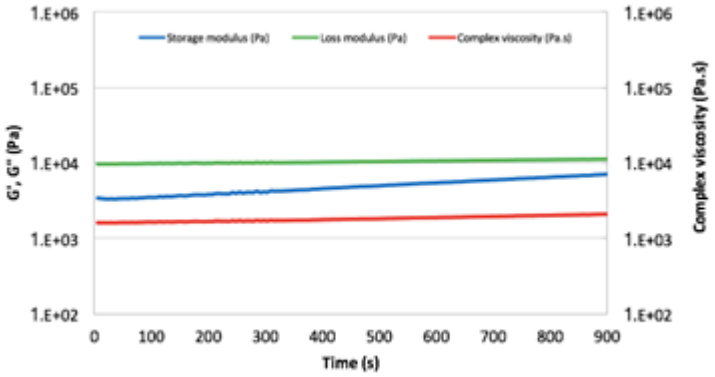

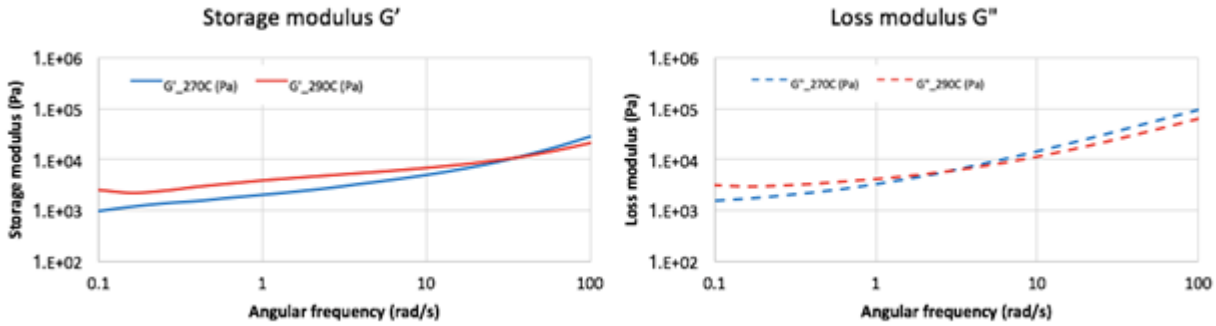

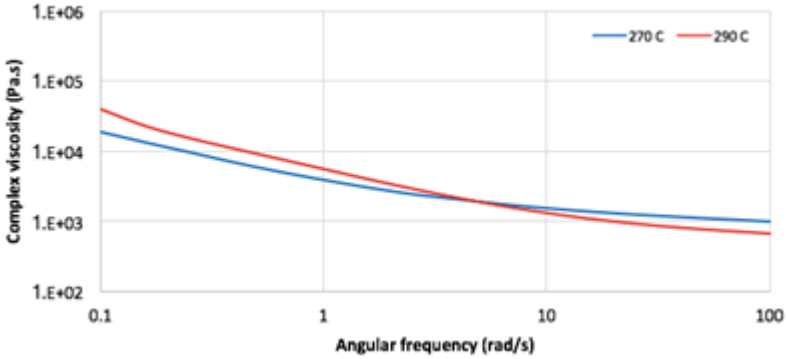

A.3 Sample 12: 30% CF/ 20% Proprietary/ PA6

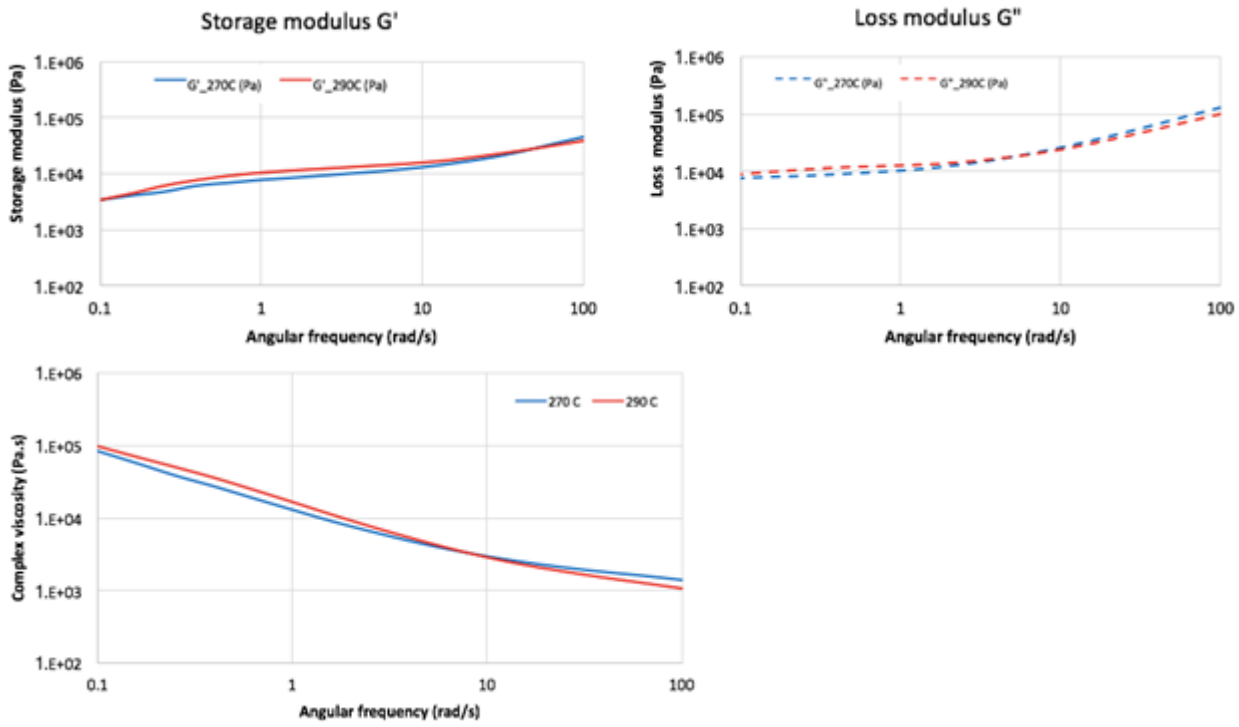

A.4 Sample 13: 10% CF/ 20% GF/ PA66

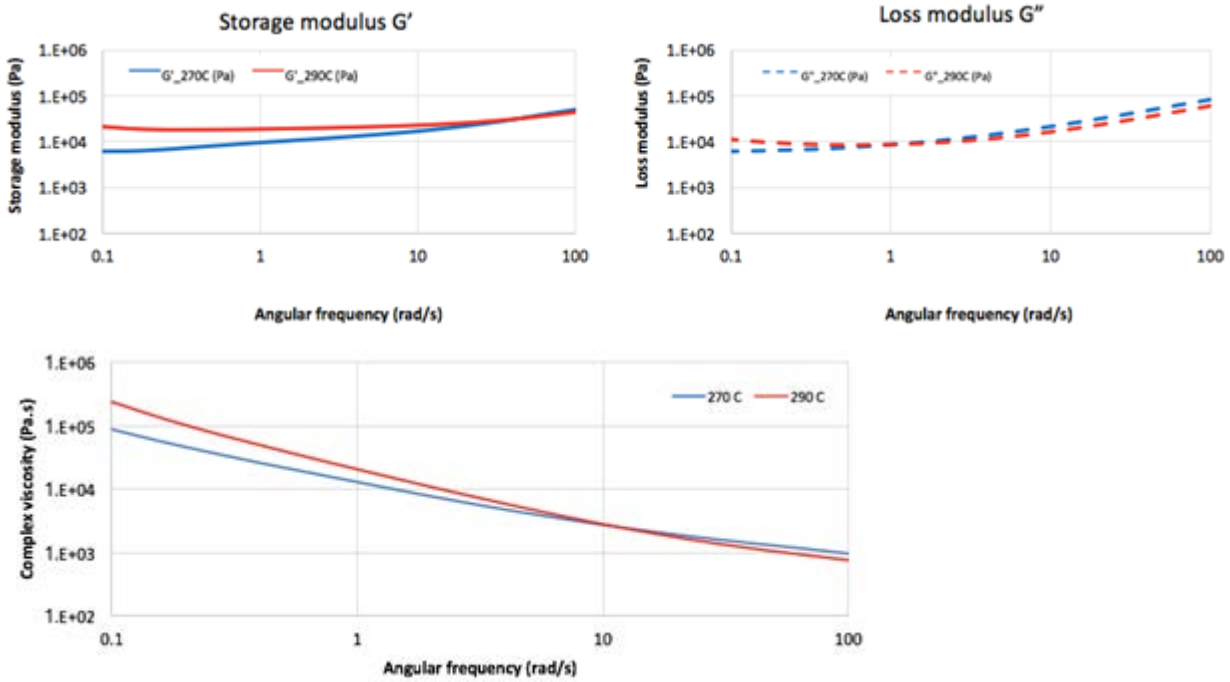

APPENDIX B: Thermo-Mechanical Analysis

B.1 Sample 1: 20% CF/ ABS

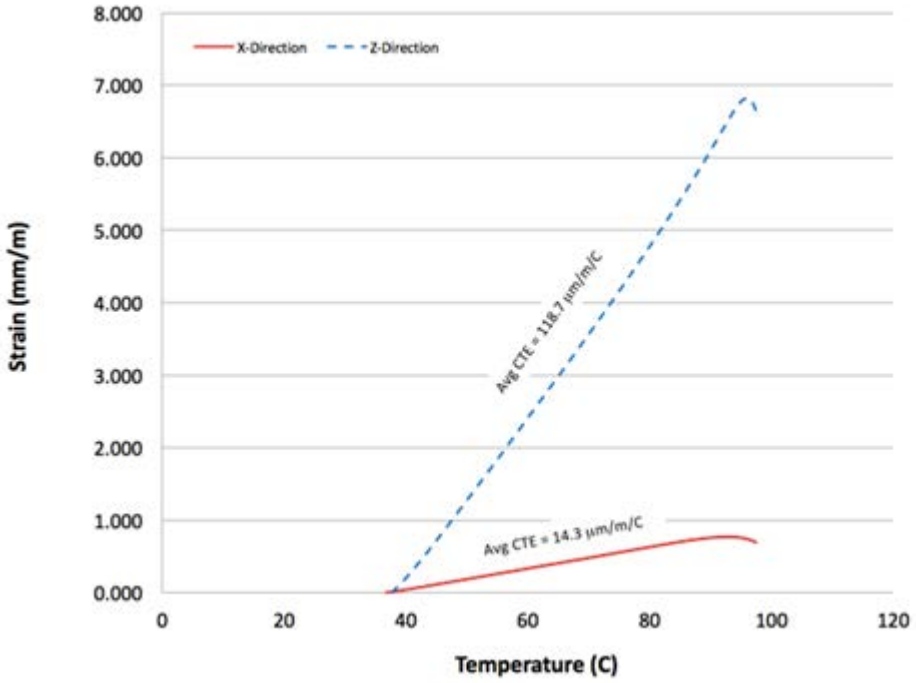

B.2 Sample 3: 20% CF/ ABS (100% recycled)

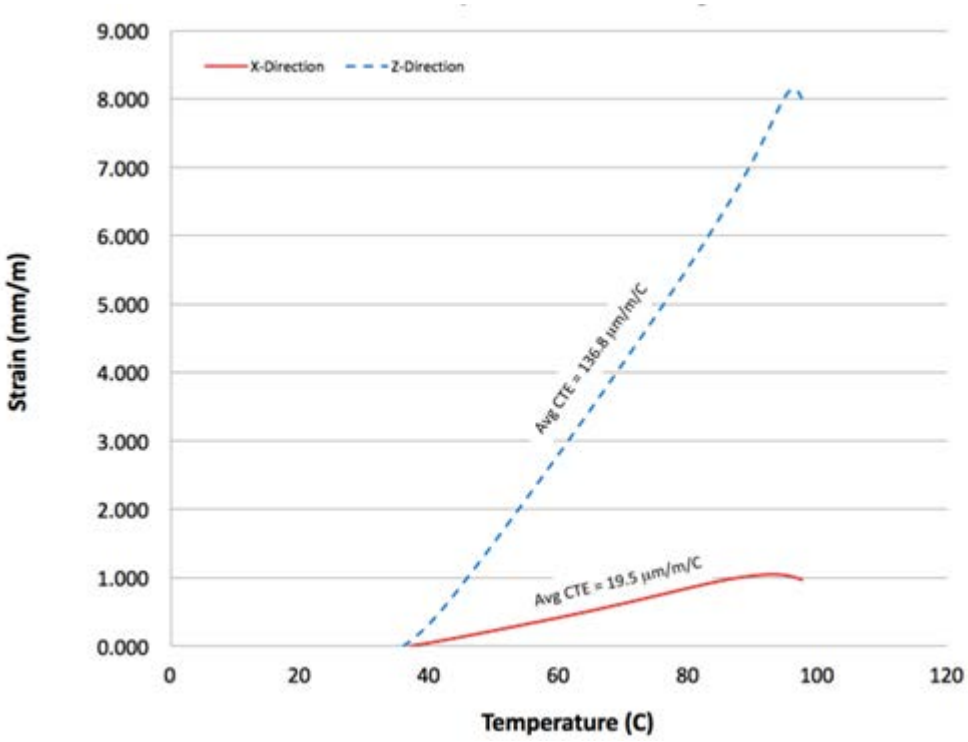

B.3 Sample 11: 20% CF/ 25% Proprietary/ PA6

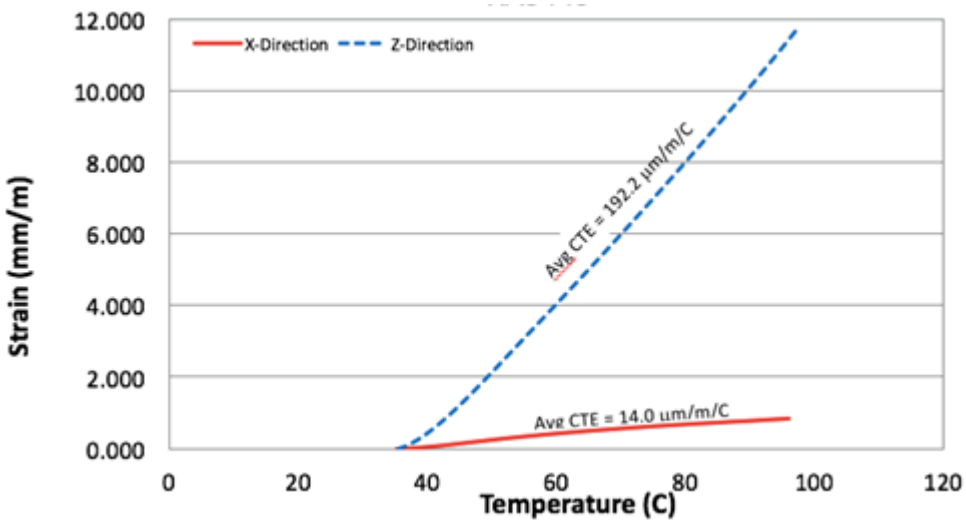

B.4 Sample 12: 30% CF/ 20% Proprietary/ PA6

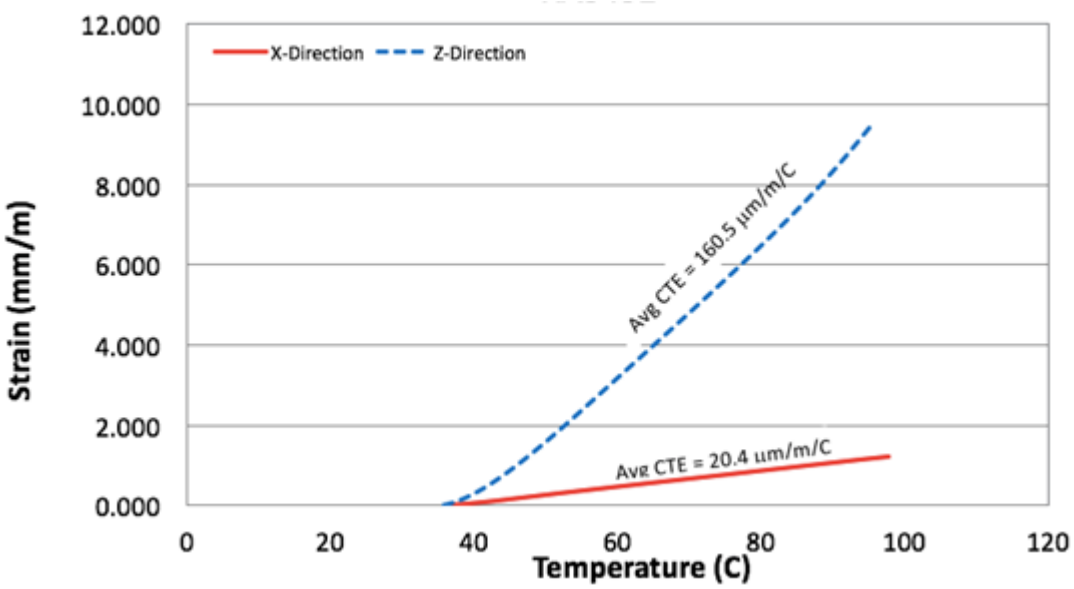

B.5 Sample 13: 10% CF/ 20% GF/ PA66

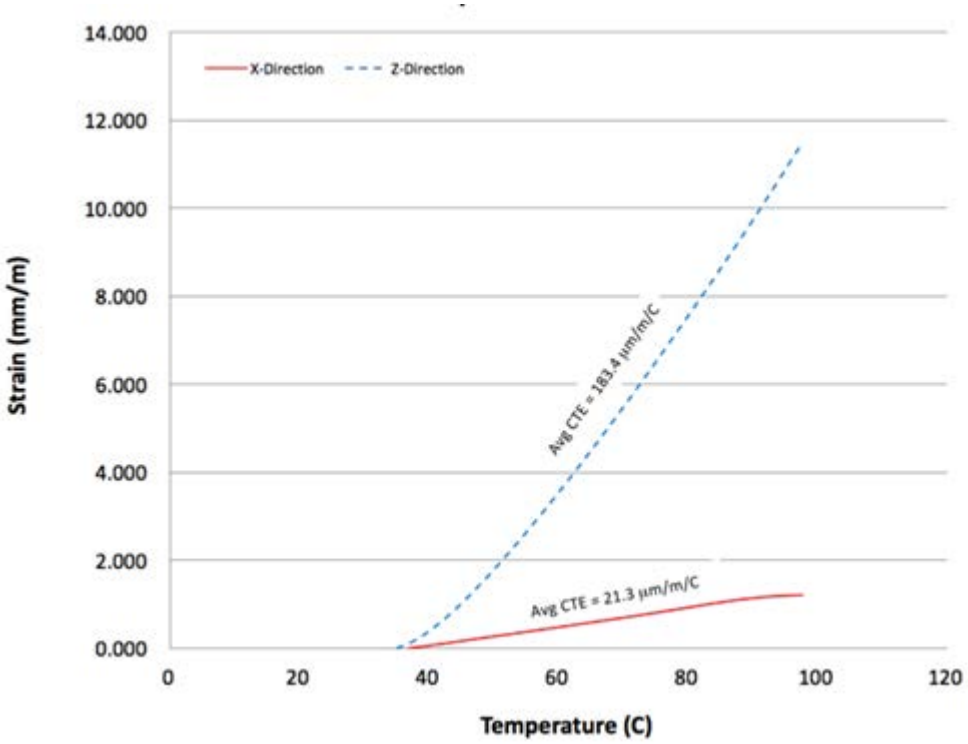

B.6 Sample 14: 20% CF/ PPE

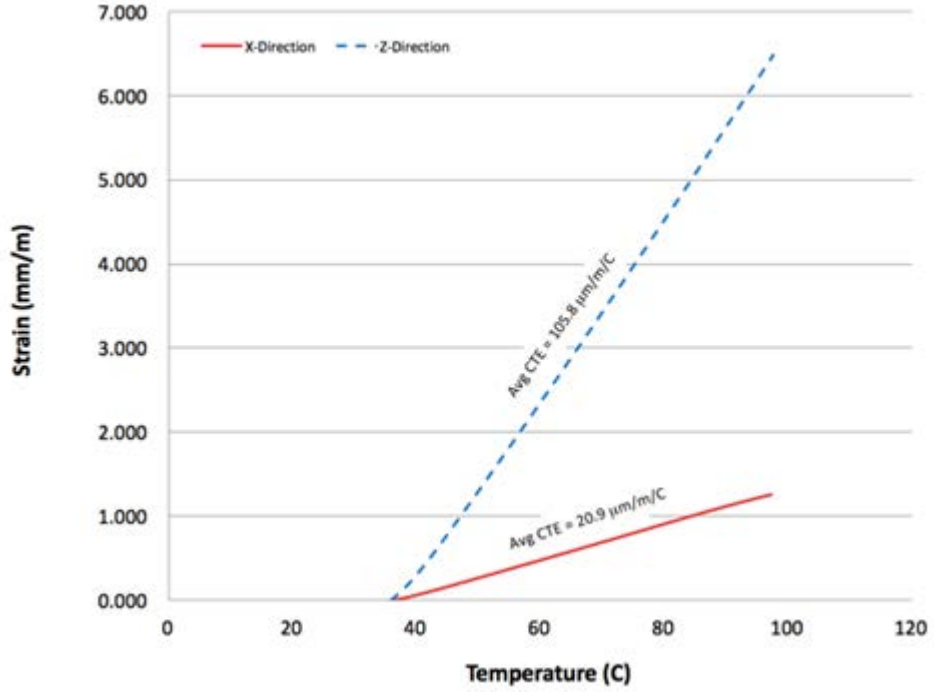

B.7 Sample 15: 20% GF/ PPE

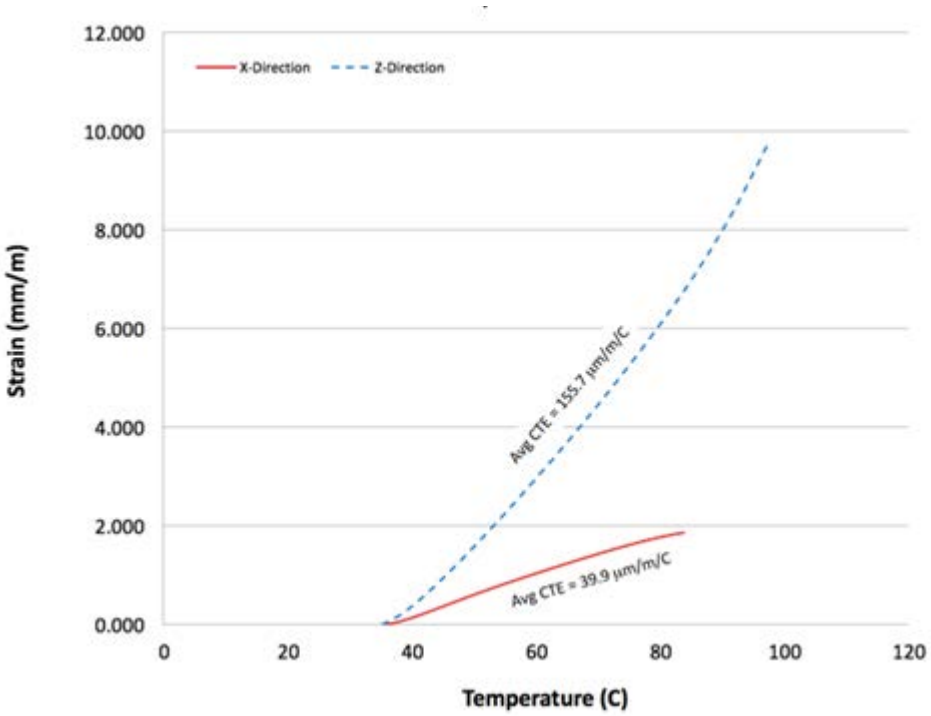

B.8 Sample 16: 20% CF/ PC

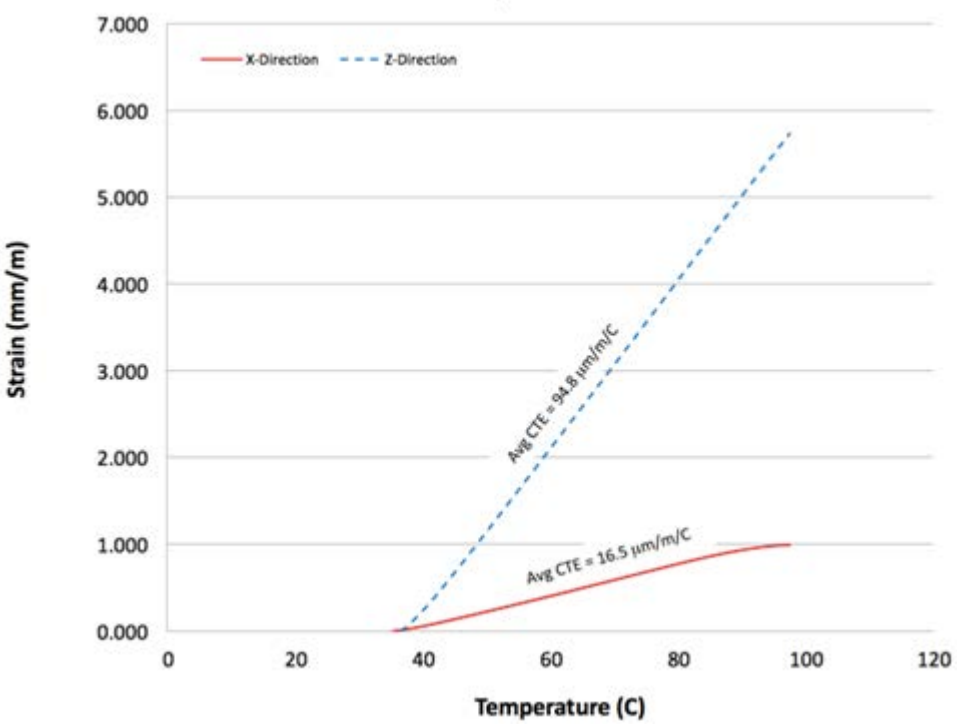

APPENDIX C: Digital Image Correlation

4-Point Bend DIC Strain Comparison at 26.7 kN

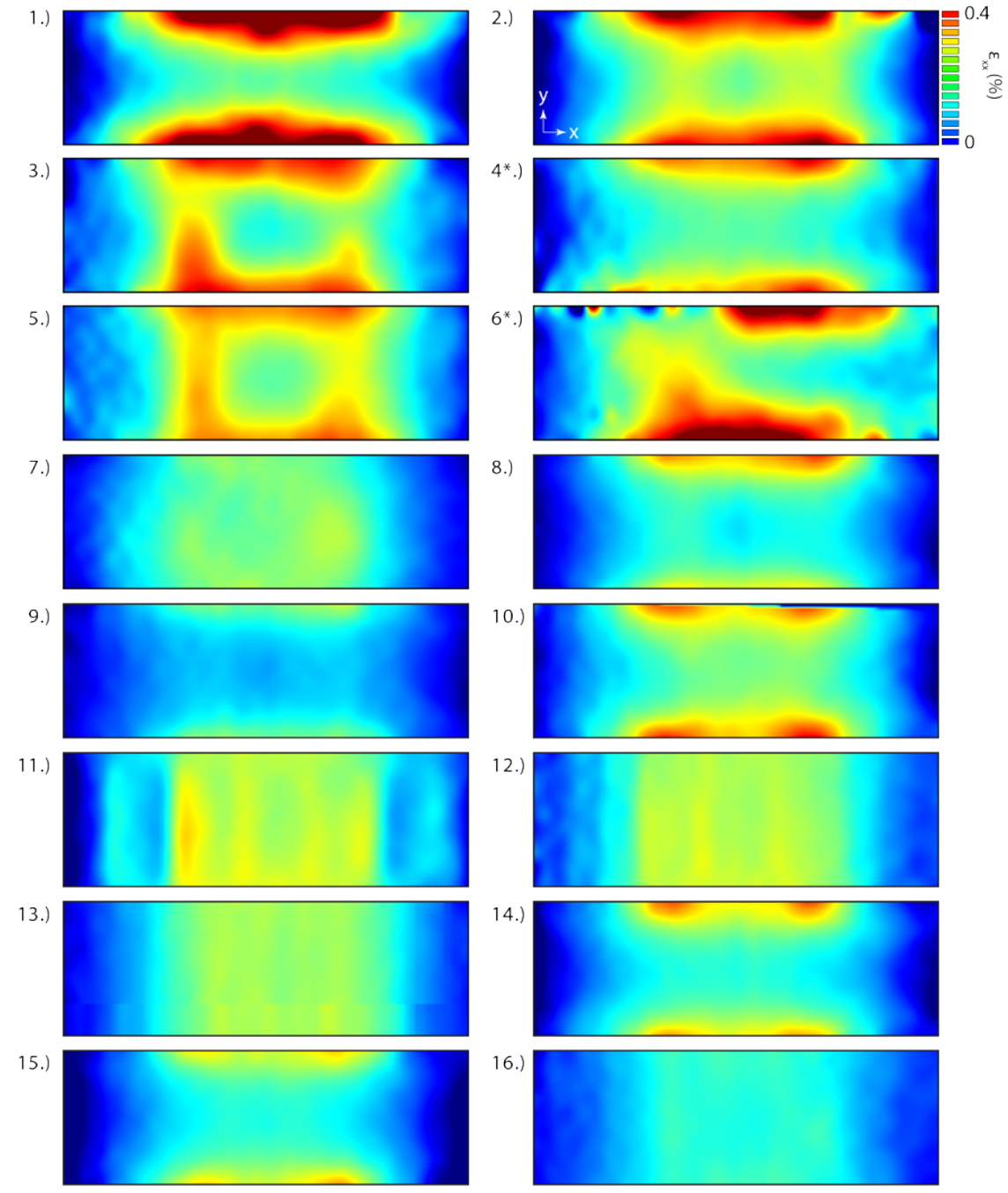

* Samples that failed before the comparison load. Maximum values for these samples are given below.

4 = 20.2 kN

6 = 23.6 kN

4-Point Bend DIC Strain Comparison at 26.7 kN

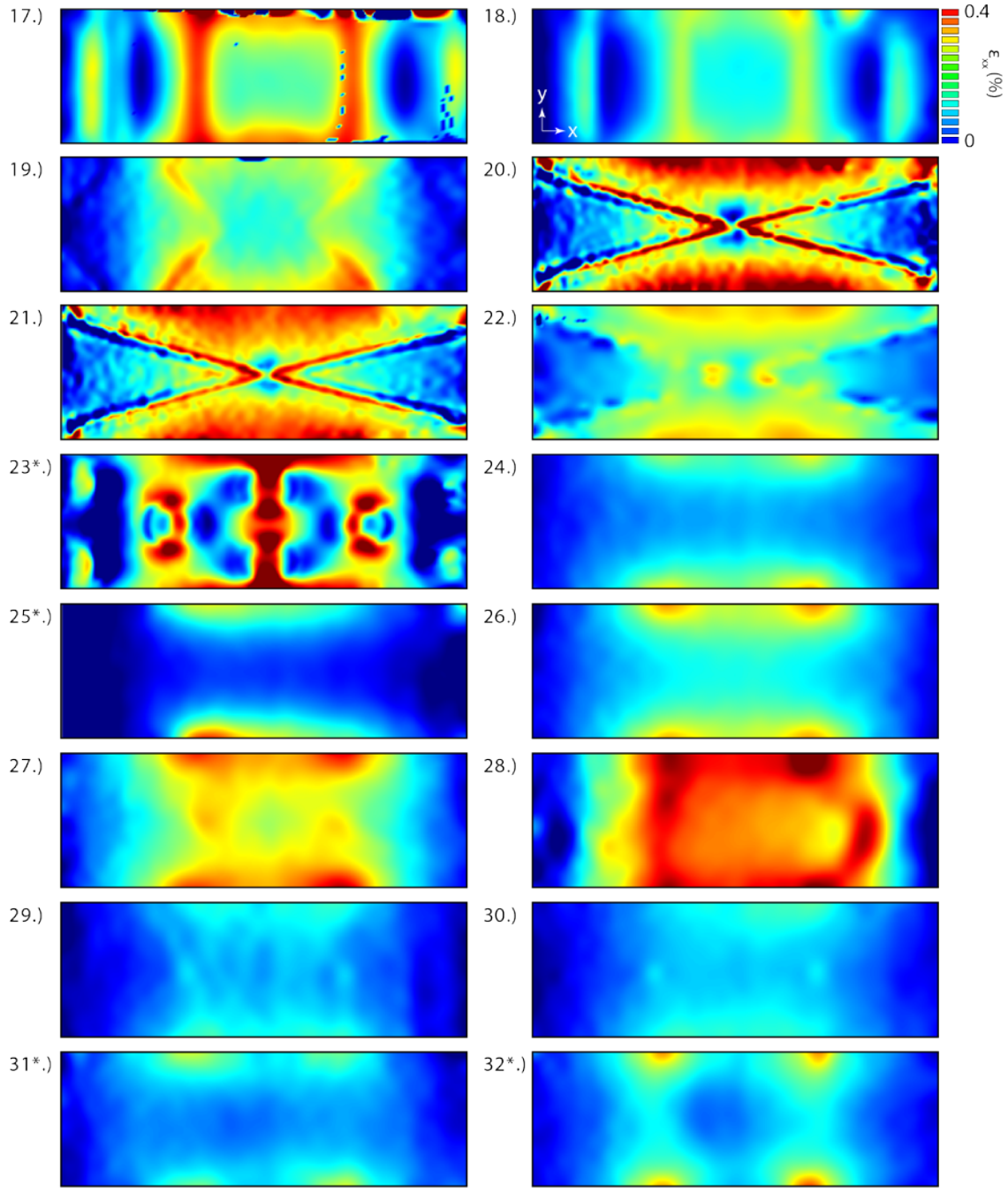

* Samples that failed before the comparison load. Maximum values for these samples are given below.

23 = 24 kN 31 = 17.8 kN

25 = 4.45 kN 32 = 24 kN

Torsion DIC Strain Comparison at 1,355 Nm

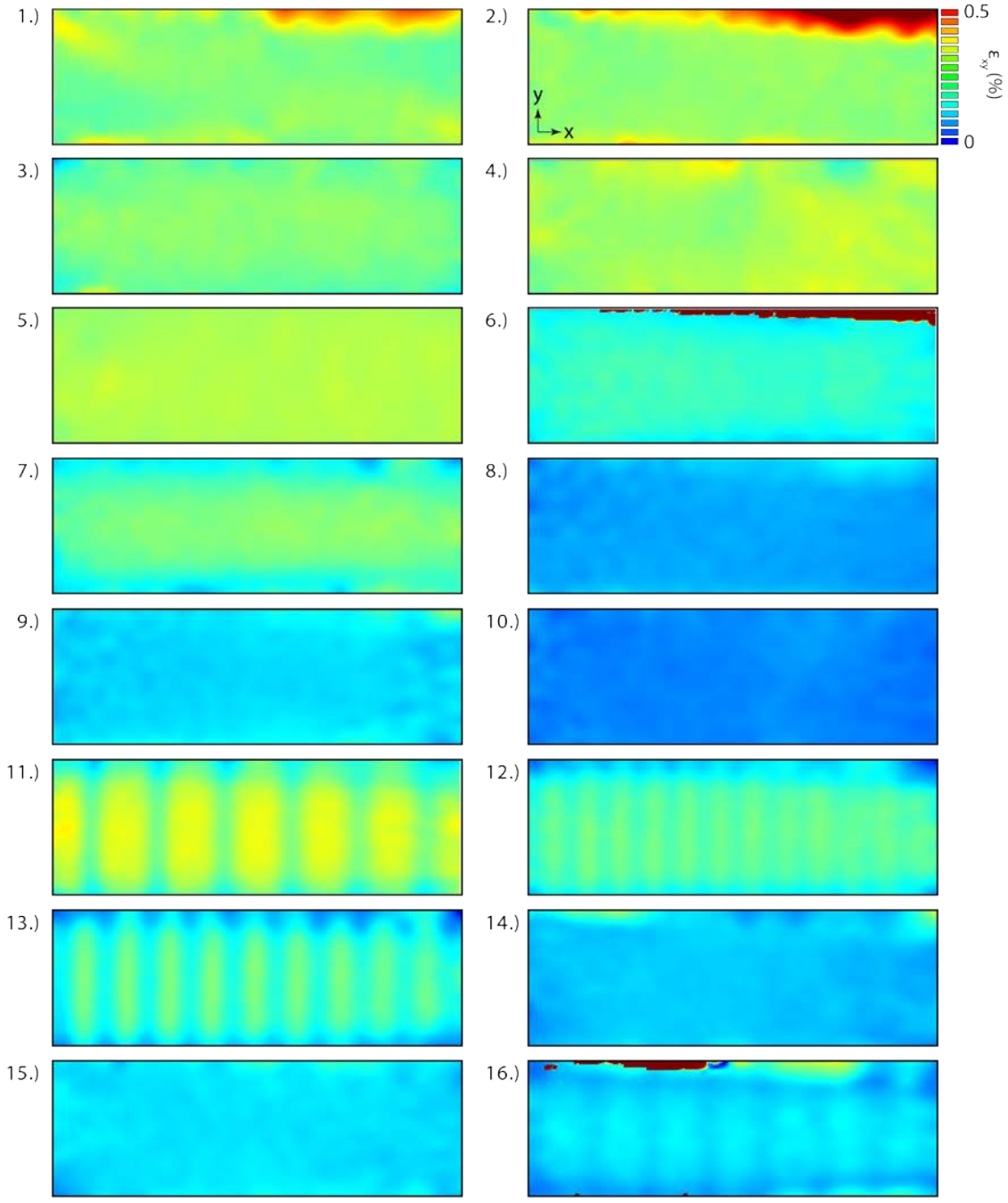

Torsion DIC Strain Comparison at 1,355 N-m

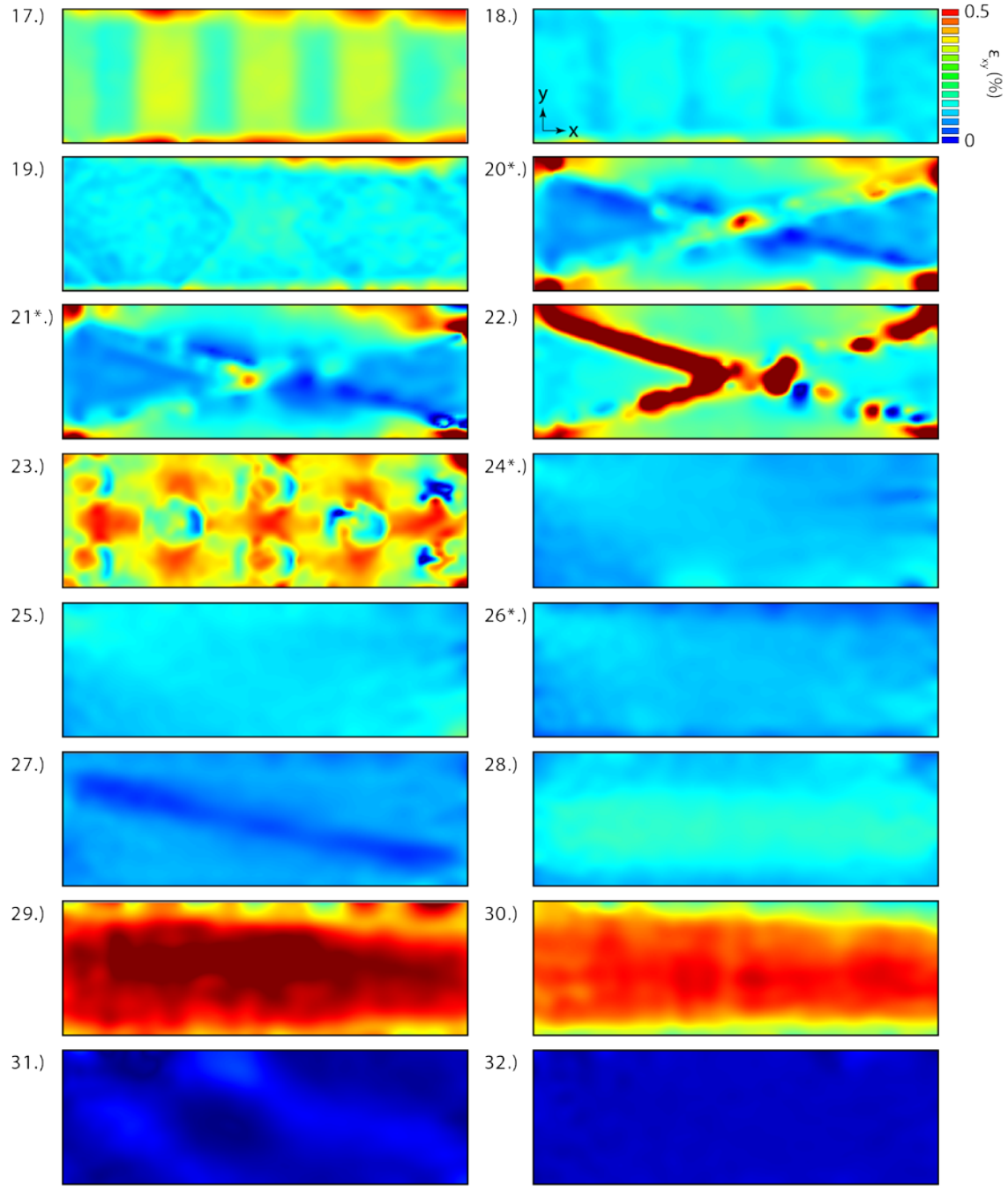

* Samples that failed before the comparison load. Maximum values for these samples are given below.

20= 908 Nm 24= 1,233 Nm

21 = 1,016 Nm 26 = 1,228 Nm

Shear DIC Strain Comparison at 88.9 kN

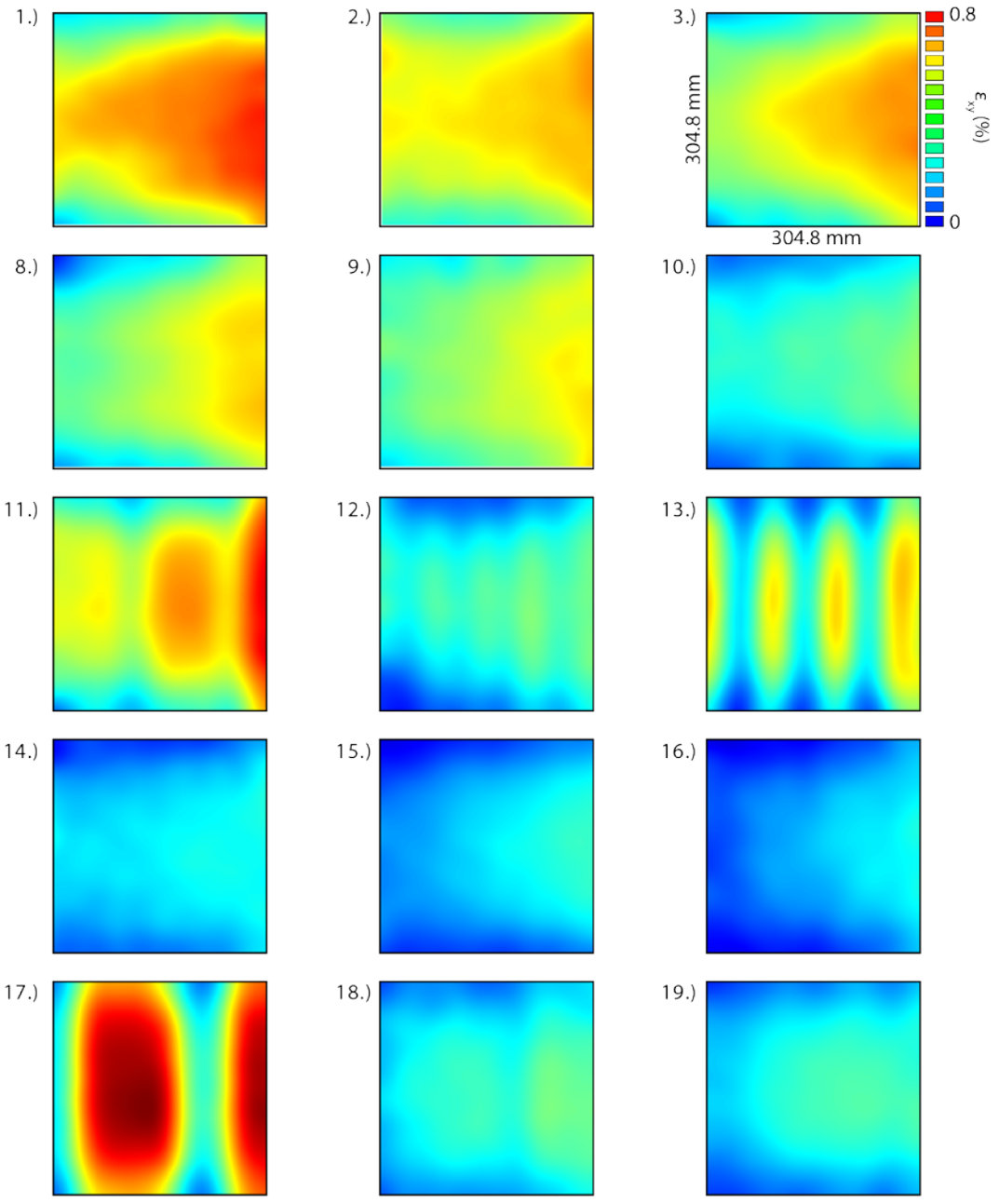

* Samples that failed before the comparison load. Maximum values for these samples are given below.
4 = 20.2 kN
6 = 23.6 kN

Shear DIC Strain Comparison at 88.9 kN

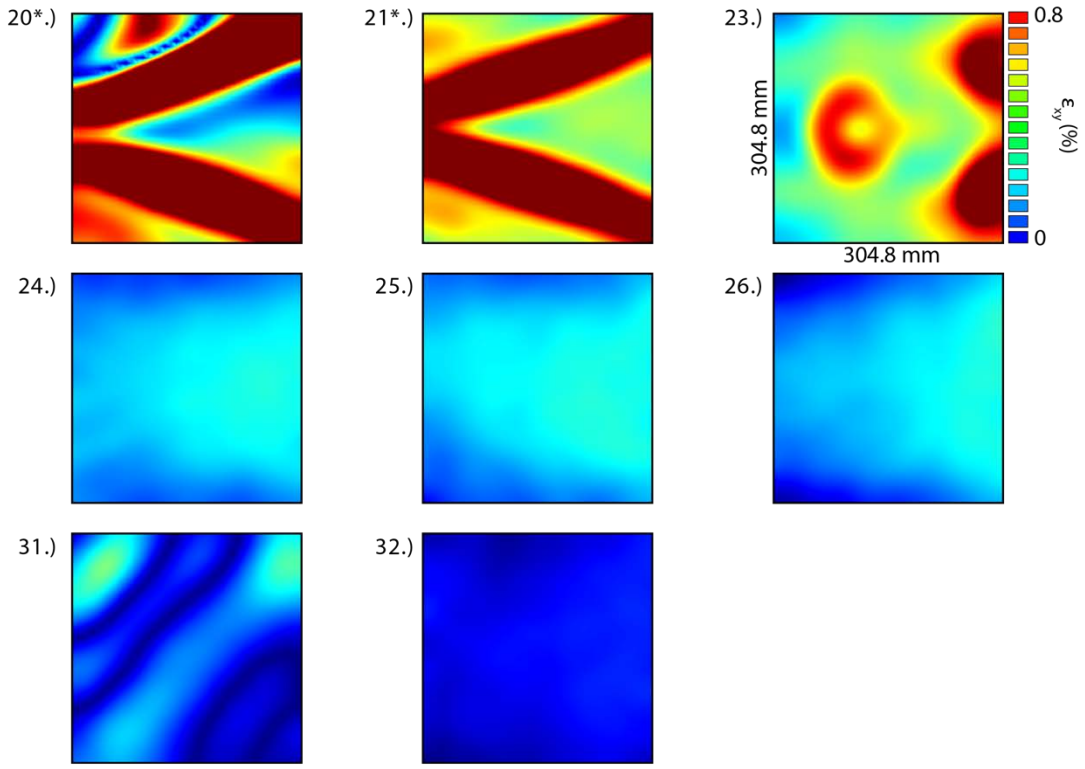

* Samples that failed before the comparison load. Maximum values for these samples are given below.
20 = 62.8 kN
21 = 66.7 kN

LIST OF ACRONYMS

AM = Additive Manufacturing
BAAM = Big Area Additive Manufacturing
CAD = Computer Aided Drafting
CF/ ABS = Carbon Fiber Acrylontrile Butadiene Styrene
CTE = Coefficient of Thermal Expansion
DDM = Direct Digital Manufacturing
DIC = Digital Image Correlation
FEA = Finite Element Analysis
IMTS = International Machine and Trade Show
IMCF = Intermediate Modulus Carbon Fiber
PA6 = Polyamide 6
PA66 = Polyamide 66
PC = Polycarbonate
PPE = Poly(p-phenylene) Ether
SMCF = Standard Modulus Carbon Fiber
TMA = Thermo-Mechanical Analysis
UTS = Ultimate Tensile Strength